

000 001 002 003 004 005 006 007 008 009 010 011 012 013 014 015 016 017 018 019 020 021 022 023 024 025 026 027 028 029 030 031 032 033 034 035 036 037 038 039 040 041 042 043 044 045 046 047 048 049 050 051 052 053 GEOMETRIC AUTOENCODER PRIORS FOR BAYESIAN INVERSION: LEARN FIRST OBSERVE LATER

Anonymous authors

Paper under double-blind review

ABSTRACT

Uncertainty Quantification (UQ) is paramount for inference in engineering applications. A common inference task is to recover full-field information of physical systems from a small number of noisy observations, a usually highly ill-posed problem. Critically, engineering systems often have complicated and variable geometries prohibiting the use of standard Bayesian UQ. In this work, we introduce Geometric Autoencoders for Bayesian Inversion (GABI), a framework for learning geometry-aware generative models of physical responses that serve as highly informative geometry-conditioned priors for Bayesian inversion. Following a “learn first, observe later” paradigm, GABI distills information from large datasets of systems with varying geometries, without requiring knowledge of governing PDEs, boundary conditions, or observation processes, into a rich latent prior. At inference time, this prior is seamlessly combined with the likelihood of the specific observation process, yielding a geometry-adapted posterior distribution. Our proposed framework is architecture agnostic. A creative use of Approximate Bayesian Computation (ABC) sampling yields an efficient implementation that utilizes modern GPU hardware. We test our method on: steady-state heat over rectangular domains; Reynold-Averaged Navier-Stokes (RANS) flow around airfoils; Helmholtz resonance and source localization on 3D car bodies; RANS airflow over terrain. We find: the predictive accuracy to be comparable to deterministic supervised learning approaches in the restricted setting where supervised learning is applicable; UQ to be well calibrated and robust on challenging problems with complex geometries. The method provides a flexible geometry-aware train-once-use-anywhere foundation model which is independent of any particular observation process.

1 INTRODUCTION

Many important problems in engineering deal with spatially varying quantities that must be inferred. The task of inferring full-field information from sparse noisy measurement is a type of inverse problem (Kaipio & Somersalo, 2005); these often need to be regularized due to their inherent ill-posedness (Calvetti & Reichel, 2003). Statistically interpretable regularization can be achieved through the Bayesian paradigm (Stuart, 2010), where we combine a likelihood function characterizing data fit for a particular observation process, and a prior which characterizes assumptions about the data-generating process. Bayesian inference allows for robust and principled uncertainty quantification, where we obtain a distribution on the estimated quantity of interest given data from a particular physical system. The main challenge in enacting a Bayesian program is prior specification; often, not much can be said about the prior which often leads to diffuse and vague posteriors with relatively poor predictive accuracy when compared to deterministic methods. To alleviate this vagueness, one possible strategy is to learn a suitable prior from a dataset of related but distinct physical setups, where more data may be available. This is explored in general-purpose AI applications (Shwartz-Ziv et al., 2022; Feng et al., 2023; Boys et al., 2024) and physical applications (Meng et al., 2022; Akyildiz et al., 2025; Patel & Oberai, 2021; Patel et al., 2022; Laloy et al., 2018; 2017). However, in engineering, *geometry* plays a crucial role in determining the dynamics arising for a physical system. Hence, for truly general purpose, practical methodology, learned priors must incorporate knowledge about the geometry of the problem at hand. But changing geometries hinder the direct learning of a prior over fields as the probability spaces involved are tied to the geometry of each individual physical system, prohibiting a direct Bayesian treatment.

In this work, we propose a methodology using graph autoencoders to learn highly informative priors as geometry-aware generative models for use in Bayesian inversion tasks. We also show how to effectively solve the Bayesian inverse problems resulting from these priors through a pushforward model. Importantly, the proposed scheme decouples the task of “learning” and the task of “inferring from observations”, resulting in train-once use everywhere approach which is independent of the particular observation process for solving inverse problems, a trait not shared by related supervised learning approaches. We make the following contributions:

- (C1) We propose a methodology to encode geometries and physical fields into a learned latent prior without specifying the governing PDE or boundary conditions.
- (C2) We prove that solving the Bayesian inverse problem in the learned latent representation solves the same problem as the inversion in the original space with a pushforward prior.
- (C3) The proposed methodology is naturally extended to the Bayesian estimation of further important information on the observation process, such as learning the observational noise.
- (C4) We test the proposed methodology on: a steady-state heat problem, RANS flow around airfoils of varying geometries, damped Helmholtz resonance and source localization on car geometries. We compare our methods to supervised neural network-based methods and Graph Gaussian Processes where relevant.
- (C5) We demonstrate the scalability of the method on a large terrain flow problem through a multi-GPU implementation; showing potential for training GABI foundation models.

Section 1.1 discusses the inference setup in detail; Section 1.2 goes over relevant related works; Section 2 describes the proposed methodology; Section 3 discusses the implementation of the proposed method; Section 4 tests and compares the proposed method; Appendices A, B, C, elaborate on proofs, additional numerical results and implementation details, relevant discussions on VAEs.

1.1 SETUP

Let $u_n \in \mathcal{U}_n := \mathcal{U}(\mathcal{M}_n; \mathbb{R}^{d_u})$ be a (possibly vector valued) function representing the full field behavior of a physical system on the bounded domain $\mathcal{M}_n \subset \mathbb{R}^d$. The space \mathcal{U} is the relevant function space for the full field solution, e.g. a Sobolev space, and the geometric domain \mathcal{M}_n may be a manifold with boundary or a boundaryless closed manifold. In this work, u_n will be: heat on a surface, fluid flow in a domain, and resonance patterns on an object. Here, the index n refers to the different physical systems which possibly have different geometries, forcing, and boundary conditions. In numerically representing these continuous systems, we obtain discretized node values $\mathbf{u}_n \in \mathcal{U}_n := \mathcal{U}(\mathcal{M}_n; \mathbb{R}^{d_u})$ which live on $\mathcal{M}_n = (\mathcal{V}_n, \mathcal{E}_n)$ where $\mathcal{V}_n = \{x_1, \dots, x_{d_n}\} \subset \mathcal{M}_n$ is a set of vertices and \mathcal{E}_n is a set of edges connecting the vertices. As such, we represent \mathcal{M}_n as an undirected graph describing the physical geometries on which the physics is taking place, i.e., a computational mesh. We assume to have a dataset $\mathcal{D} = \{\mathbf{u}_n, \mathcal{M}_n\}_{n=1}^N$ ¹. This dataset can be constructed from simulation data, as is the case in this paper, or from full-field data from experiment such as through particle image velocimetry, digital image correlation, magnetic resonance, electrical impedance tomography, infrared thermography etc.

First, in the proposed methodology we learn a \mathcal{M}_n -dependent prior generative model for \mathbf{u}_n . Second, using this learned highly informative prior and *sparse* *noisy* observations, $\mathbf{y}_o \in \mathbb{R}^{d_o}$ ², of a new physical system on a new geometry, \mathcal{M}_o , we solve the Bayesian inverse problem to obtain the posterior distribution $p_{\mathbf{u}_o | \mathbf{y}_o}$. We assume to know the discretized geometry \mathcal{M}_o associated to \mathbf{y}_o . In this paper, the observations and discretized solution field are related by:

$$\mathbf{y}_o = \mathbf{H}_o \mathbf{u}_o + \boldsymbol{\xi}_o, \quad \boldsymbol{\xi}_o \sim \mathcal{N}(\mathbf{0}, \sigma^2 \mathbf{I}_o). \quad (1)$$

We take $\mathbf{H}_o : \mathbb{R}^{d_u} \rightarrow \mathbb{R}^{d_o}$ to be a matrix of zeros and ones selecting the nodes to be observed. This is assumed to be a known observation operator corresponding to sensor placements. We note that many observation models can be considered with ease, such as surface integrals for computing drag coefficients, radon transforms for tomography, as well as any number of noise models – additive or not. As our learned prior is entirely independent of the observation process, changes to the observation process do not necessitate retraining and can be incorporated “on-the-fly”.

¹A dataset with multiple full-fields per geometry \mathcal{M}_n , as $\{\{\mathbf{u}_{n,i}\}_{i=1}^{N_n}, \mathcal{M}_n\}_{n=1}^N$, can be viewed as a dataset $\{\mathbf{u}_k, \mathcal{M}_k\}_{k=1}^K$ indexed by a dummy variable k such that k maps to (i, n) .

²When discussing observations which are associated to a geometry not in the dataset \mathcal{D} we change the index from n to o for clarity.

108 The proposed methodology works as follows:
 109

- 110 In the training stage, using a dataset of geometries and full-field solutions on these geometries, $\mathcal{D} = \{\mathbf{u}_n, \mathbf{M}_n\}_{n=1}^N$, we learn a graph autoencoder which embeds the joint distribution
 111 of solutions and geometries into a latent Gaussian distribution. This will act as our highly
 112 informative geometry-aware data-driven prior.
- 113 In the application stage, we use this learned prior to solve inverse problems for data coming
 114 from new physical systems not in the dataset \mathcal{D} . That is, given *sparse and noisy* observations
 115 \mathbf{y}_o of a solution \mathbf{u}_o of a physical systems with geometry \mathbf{M}_o , we use our previously learned
 116 prior to solve the Bayesian inverse problem for the unknown full-field \mathbf{u}_o . We recover a
 117 distribution over the solution \mathbf{u}_o by only observing \mathbf{y}_o .

118 Using the proposed methodology, one can encode prior beliefs through geometry-dependent full-field
 119 solution datasets. Practitioners can then construct highly-informative priors from data across varying
 120 physical geometries. This prior is independent of the observation process for any particular inference
 121 task, hence this is a learn-once apply everywhere approach.

123 1.2 RELATED WORKS

125 1.2.1 DIRECT MAP INVERSION

127 Many interesting approaches have been recently proposed which directly learn an amortized map
 128 from observable to solution/parameter. These can be subdivided into deterministic methods and
 129 probabilistic - often Bayesian - approaches. Most related to the setting considered in this paper
 130 is the work in Duthé et al. (2025). Here, the authors consider a graph-ML approach to learning a
 131 deterministic map from observable \mathbf{y}_o to the underlying vector field \mathbf{u}_o . The supervised methodology
 132 used in the comparisons in this work draws inspiration from that prior work. Another strongly related
 133 methodology can be found in Arridge et al. (2019) although here the problem of changing geometry
 134 is not directly tackled. Other noteworthy works in this area include (Adler & Öktem, 2017; Dittmer
 135 et al., 2020). Interesting works look at probabilistic schemes for constructing probabilistic maps from
 136 observable to quantity of interest (Kaltenbach et al., 2023; Baptista et al., 2024). These works do not
 137 focus on learning priors. Other works in this area include (Adler et al., 2022; Ardizzone et al., 2018).

138 1.2.2 FORWARD AND INVERSE PROBLEMS ON GRAPHS

139 Graphs are handled in machine learning frameworks through geometric deep learning (Bronstein
 140 et al., 2021; Wu et al., 2022; Kipf, 2016). Several important works consider inverse problems where
 141 the quantity inferred lives of a graph description of the geometry. In Garcia Trillo & Sanz-Alonso
 142 (2018) the authors prove the convergence of the graph posterior to the continuum posterior subject to
 143 some conditions. In Povala et al. (2022) the adjacency structure of a mesh is leveraged to accelerate
 144 variational inference inversion. Important works consider solving the PDE forward problem through
 145 physics informed graph machine learning (Seo & Liu, 2019; Valencia et al., 2025; Wandel et al., 2020)
 146 Used in our comparisons are linear inverse problems with Gaussian process priors, this leads to graph
 147 Gaussian process methods (Borovitskiy et al., 2021; Mostowsky et al., 2024). We find it important
 148 to mention important works in the physics informed literature, where assuming complete or partial
 149 knowledge on PDEs, boundary conditions, forcing etc, one can use physics residuals to learn forward
 150 and inverse maps for PDEs (Raissi et al., 2019; Gao et al., 2022; Vadeboncoeur et al., 2023; Xu et al.,
 151 2023; Rixner & Koutsourelakis, 2021). However, in this work, we focus solely on methods which
 152 do not assume knowledge of the governing PDE, boundary conditions, or forcing and are entirely
 153 data-driven in their approach.

154 1.2.3 STATISTICAL AUTOENCODERS

156 Related to inverse problem are latent variable representations of graph data structures. In this category
 157 the seminal work of the graph VAE (Kipf & Welling, 2016; Nazari et al., 2023). We refer the reader
 158 to Appendix C for a more elaborate discussion on the relationship between VAEs and our proposed
 159 framework. Related to this are the works (Mylonas et al., 2021; Liu et al., 2019). The proposed
 160 work centres around a class of autoencoders dubbed statistical autoencoders, of which there are
 161 many variants (Zhao et al., 2019; Kolouri et al., 2019; Turinici, 2021; Tolstikhin et al., 2018). We
 162 specifically focus on the MMD (Gretton et al., 2012) variant of the autoencoder. Many other variants

162 could be considered. Another relevant class of autoencoders are conditional autoencoders (Sohn
 163 et al., 2015), we will make use of related ideas by conditioning encoder and decoder on geometry.
 164

165 **1.3 NOTATION**

166 We denote by \mathbb{P}_z a probability measure on the measurable space $(\mathcal{Z}, \mathcal{S})$, and by p_z the associated
 167 density with respect to Lebesgue measure when it exists. Empirical measures are a mixture of
 168 Dirac measures. That is, for $D = \{x_i\}_{i=1}^M$, we have $\widehat{\mathbb{E}}_{x \in D}[\delta_x] = \frac{1}{M} \sum_{i=1}^M \delta_{x_i}$, where $\delta_{x_i}(A) =$
 169 1 if $x_i \in A$, and $\delta_{x_i}(A) = 0$, if $x_i \notin A$. We will sometimes refer to mixtures of Diracs measures as
 170 the “densities” p, q to lighten notation. Superscripts in parentheses denote realizations of random
 171 variables. For a function $g : \mathcal{Z} \rightarrow \mathcal{U}$, the pushforward $g_\# p_z$ means $g_\# \mathbb{P}_z(A) = \mathbb{P}_z(g^{-1}(A))$ for all
 172 measurable sets A . We note, a sample $u^{(n)} \sim g_\# p_z$ is obtained as $u^{(i)} = g(z^{(i)})$, $z^{(i)} \sim p_z$.
 173

174 **2 METHODOLOGY**

175 We now describe the proposed methodology in detail. In Section 2.1 we carefully layout the central
 176 result allowing for the Bayesian treatment of the inference task; that is, the equivalence between the
 177 Bayesian posterior of a pushforward prior (our generative model), and the Bayesian inverse problem
 178 in the implied latent space of the pushforward prior. Following from this result, in Section 2.2 we
 179 describe our two-step procedure: first, learn a generative model to be used as a Geometry-conditioned
 180 Bayesian prior; second, observe sparse data for the inverse problem and solve the Bayesian inverse
 181 problem in the latent space to push this posterior back out to the desired physical field living on the
 182 geometry of interest. In Section 2.3 we show how to extend our methodology to estimate the noise in
 183 the observations.
 184

185 **2.1 POSTERIOR FROM A PUSHFORWARD PRIOR**

186 We present the lemma motivating our methodology; the equivalence between the Bayesian posterior
 187 with a pushforward latent prior and the pushforward of the Bayesian posterior over the latent space.
 188

189 **Lemma 2.1.** *Let $(\mathcal{U}, \mathcal{F}, \mathbb{P}_u)$, and $(\mathcal{Z}, \mathcal{S}, \mathbb{P}_z)$ be measure spaces and $g : \mathcal{Z} \rightarrow \mathcal{U}$ be $(\mathcal{S}, \mathcal{F})$ -
 190 measurable. Furthermore, let $\mathbb{P}_{u|y}$ be the Bayesian posterior on \mathcal{U} with likelihood proportional to
 191 $\exp(-\Phi(u; y))$ and prior $\mathbb{P}_u := g_\# \mathbb{P}_z$. We find*

$$192 \mathbb{P}_{u|y} = g_\# \mathbb{P}_{z|y},$$

193 where $d\mathbb{P}_{z|y}(z) = 1/Z(y) \exp(-\Phi(g(z); y)) d\mathbb{P}_z(z)$ is the Bayesian posterior on \mathcal{Z} .

194 Stated simply, in Bayesian inference, when a prior on \mathcal{U} is specified as the pushforward under g
 195 (Subsection 1.3) of a latent prior on a space \mathcal{Z} , two distributions are equivalent: i) the Bayesian
 196 posterior on \mathcal{U} , and ii) the pushforward under g of the posterior associated to the latent prior on \mathcal{Z} .
 197 This result will be explicitly related to the geometric inference setting in Theorem 2.2, showing that
 198 with a latent prior constructed via a geometry aware encoder/decoder, we can solve inverse problems
 199 on \mathcal{U} with a single common latent representation relevant to any number of in-distribution geometries.
 200 All proofs can be found in Appendix A.

201 **2.2 GEOMETRIC AUTOENCODER PRIORS FOR BAYESIAN INVERSION (GABI)**

202 We describe the two-step process of learning a geometry-aware prior and how to use this to solve
 203 inverse problems.

204 **Step 1: Learn Geometric Autoencoder Prior.** Let $\mathbf{z} \in \mathcal{Z} = \mathbb{R}^{d_z}$ be a latent vector. We pose the
 205 \mathcal{M}_n -dependent maps

$$206 E_n^\theta : \mathcal{U}_n \rightarrow \mathcal{Z}, \quad \text{where} \quad E_n^\theta(\mathbf{u}_n) := E^\theta(\mathbf{u}_n; \mathcal{M}_n); \quad (2a)$$

$$207 D_n^\psi : \mathcal{Z} \rightarrow \mathcal{U}_n, \quad \text{where} \quad D_n^\psi(\mathbf{z}) := D^\psi(\mathbf{z}; \mathcal{M}_n). \quad (2b)$$

208 Both E^θ (the encoder) and D^ψ (the decoder) are graph neural networks with parameter sets θ, ψ
 209 respectively. These two maps imply a geometry conditioned autoencoder. We use $\widehat{\mathbb{E}}_{\mathcal{D}}[\cdot]$ as a

216 shorthand for $\frac{1}{N} \sum_{(\mathbf{u}_n, \mathbf{M}_n) \in \mathcal{D}} [\cdot]$. Set the parameters of the auto-encoder to
 217

$$218 \quad \theta^*, \psi^* = \arg \min_{\theta, \psi} \widehat{\mathbb{E}}_{\mathcal{D}} [\|\mathbf{u}_n - (D_n^\psi \circ E_n^\theta)(\mathbf{u}_n)\|_2^2] + d(p_{\mathbf{z}}^\theta, q_{\mathbf{z}}), \quad (3)$$

220 where $p_{\mathbf{z}}^\theta = \widehat{\mathbb{E}}_{\mathcal{D}} [\delta_{E_n^\theta(\mathbf{u}_n)}]$ is the empirical distribution of encoded solutions, $q_{\mathbf{z}} = \mathcal{N}(\mathbf{0}, \mathbf{I})$, $\arg \min$
 221 is to be approximated with gradient descent, and $d : \mathcal{P}(\mathbf{Z}) \times \mathcal{P}(\mathbf{Z}) \rightarrow [0, \infty)$ may be any suitable
 222 divergence that is well-posed for comparing empirical measures: maximum mean discrepancy
 223 (MMD), energy distance (ED), Wasserstein, or Sliced-Wasserstein distances etc. In this work, we
 224 focus on MMD.
 225

226 **Step 2: Observe and Sample Posterior.** For new data \mathbf{y}_o associated to a geometry \mathbf{M}_o , we re-write
 227 the data generating model in (1) in terms of a decoded latent variable as
 228

$$229 \quad \mathbf{y}_o = \mathbf{H}_o D_o^\psi(\mathbf{z}) + \xi_o, \quad \xi_o \sim \mathcal{N}(\mathbf{0}, \sigma^2 \mathbf{I}_o), \quad (4)$$

230 where $D_o^\psi = D^\psi(\cdot; \mathbf{M}_o)$. We specify our prior distribution over \mathbf{u}_o , denoted $p_{\mathbf{u}_o}$, using the trained
 231 decoder; and specify the likelihood, denoted $p_{\mathbf{y}_o|\mathbf{z}}^\psi$, associated to this decoded observation model (4)
 232

$$233 \quad p_{\mathbf{u}_o}^\psi := D_o^\psi \# q_{\mathbf{z}}; \quad p_{\mathbf{y}_o|\mathbf{z}}^\psi = \mathcal{N}(\mathbf{H}_o D_o^\psi(\mathbf{z}), \sigma^2 \mathbf{I}_o). \quad (5)$$

234 This likelihood along with prior $q_{\mathbf{z}}$ imply a posterior
 235

$$236 \quad p_{\mathbf{z}|\mathbf{y}_o}^\psi(\mathbf{z}) = \frac{p_{\mathbf{y}_o|\mathbf{z}}^\psi(\mathbf{y}_o) q_{\mathbf{z}}(\mathbf{z})}{p_{\mathbf{y}_o}(\mathbf{y}_o)}. \quad (6)$$

237 **Theorem 2.2.** *Assuming the relevant measurability of D_o^ψ , the posterior*

$$238 \quad p_{\mathbf{u}_o|\mathbf{y}_o}^\psi = D_o^\psi \# p_{\mathbf{z}|\mathbf{y}_o}. \quad (7)$$

239 The posterior (7) is sampled by first sampling from $p_{\mathbf{z}|\mathbf{y}_o}^\psi$ in (6) and decoding with D_o^ψ . Hence, by
 240 first solving the inverse problem in the latent space, we can use Theorem 2.2 to easily obtain posterior
 241 samples in the decoded solution space for a given geometry. This allows us to learn a unified prior
 242 over the solution field as a generative model *over varying geometries* and use it to solve Bayesian
 243 inverse problems with a highly informative learned prior on new geometries.
 244

245 2.3 OBSERVATIONAL NOISE ESTIMATION

246 Beyond the benefits of quantifying uncertainty related to model predictions, the Bayesian paradigm
 247 offers a principled framework for estimating other aspects of the data-generating model. We highlight
 248 that such estimations are completely independent of the training of the autoencoder prior – this is
 249 not the case for direct regression methods which need to have all observation variables incorporated
 250 at training time. We now consider the common task of jointly estimating the observational noise
 251 standard deviation σ_o (now indexed by o as it may vary from one system to another), together with
 252 the field of interest \mathbf{u}_o . This is achieved through the latent joint posterior
 253

$$254 \quad p_{\mathbf{z}, \sigma_o|\mathbf{y}_o}^\psi(\mathbf{z}, \sigma_o) = \frac{p_{\mathbf{y}_o|\mathbf{z}, \sigma_o}^\psi(\mathbf{y}_o) p_{\mathbf{z}, \sigma_o}(\mathbf{z}, \sigma_o)}{p_{\mathbf{y}_o}(\mathbf{y}_o)}. \quad (8)$$

255 where $p_{\mathbf{z}, \sigma_o}(\mathbf{z}, \sigma_o) = q_{\mathbf{z}}(\mathbf{z}) p_{\sigma_o}(\sigma_o)$ for a specified prior $p_{\sigma_o}(\sigma_o)$.
 256

257 **Corollary 2.3.** *We can sample the joint posterior on the solution fields through the pushforward*
 258 $p_{\mathbf{u}_o, \sigma_o|\mathbf{y}_o}^\psi = (D_o^\psi \otimes \text{Id.}) \# p_{\mathbf{z}, \sigma_o|\mathbf{y}_o}^\psi$, *where Id. is the identity map.*
 259

260 3 IMPLEMENTATION

261 **Neural Networks:** We make use of meshes and graph neural networks to describe and manipulate
 262 geometric information. The proposed methodology is agnostic to any particular architecture, however
 263 we need the following characteristics: *Geometry aware architecture and data-structure; Mapping*
 264 *to and from fixed-dimensional vectors; Non-locality.* We expand on these points in B. For the heat,
 265

270

Algorithm 1: Inversion with GABI-ABC

272 1: Specify the observation vector \mathbf{y}_o , discretized geometry \mathbf{M}_o , total sample budget N_s , number of
 273 accepted samples N_a .
 274 2: Train E^θ, D^ψ through (3) on \mathcal{D} .
 275 3: **for** [Batched/Paralelized] $i = 1 : N_s$ **do**
 276 4: Sample $\mathbf{z}^{(i)} \sim q_{\mathbf{z}}$
 277 5: Decode $\mathbf{u}_o'^{(i)} = D^\psi(\mathbf{z}^{(i)}; \mathbf{M}_o)$
 278 6: Apply observation process with noise: $\mathbf{y}_o'^{(i)} = \mathbf{H}_o \mathbf{u}_o'^{(i)} + \xi_o'^{(i)}; \quad \xi_o'^{(i)} \sim \mathcal{N}(\mathbf{0}, \sigma^2 \mathbf{I}_o)$.
 279 7: Compute $r_i = \|\mathbf{y}_o - \mathbf{y}_o'^{(i)}\|_2$.
 280 8: **return** return N_a samples of $\mathbf{u}_o^{(1:N_s)}$ with least residual r_i .

281

282

283 airfoil, and car problems we make use of a Graph Convolutional Network with interleaved nonlocal
 284 averaging layers (Lanthaler et al., 2024). For the terrain flow problem we use a GEN (Li et al., 2020)
 285 GNN architecture. We detail these architectures in Appendix B.1. We also test a Transformer on the
 286 heat problem in Appendix B.3.3.

287

Sampling: To realize GABI, we first train the autoencoder; then, we sample from the corresponding
 288 latent posterior as in (6) and decode the resulting latent samples to obtain samples from the posterior
 289 for a given geometry. We note two alternatives for sampling from the posterior: MCMC, and
 290 ABC sampling. We find ABC sampling to be advantageous for this task due to: (i) the massive
 291 parallelization capabilities of neural networks as opposed to the sequential nature of MCMC; (ii)
 292 the specification of a well-tailored prior distribution – the prior is not unnecessarily vague leading
 293 to good overlap between the prior and posterior; (iii) the low dimensionality of the observational
 294 data – removing the need to use possibly problematic summary statistics. In Algorithm 1 we
 295 outline the implementation of the GABI-ABC variant. For MCMC sampling, we use the NUTS
 296 algorithm (Hoffman et al., 2014).

297

Notes on Alternative Approaches: Physics Driven Inversion. These require additional knowledge
 298 aside from access to a representative dataset and information specific to each system we wish to
 299 query such as the governing PDE, boundary conditions, forcing etc. **VAEs.** We refer the reader
 300 to Appendix C for an in-depth discussion on the unsuitability of VAEs for the task we are solving,
 301 both in terms of the overall methodology and in terms of the autoencoder used within the proposed
 302 methodology. **Supervised learning/Direct Map Inversion.** One can choose to learn a supervised
 303 learning direct mapping $(\mathbf{y}_n, \mathbf{M}_n) \mapsto \mathbf{u}_n$; this approach is the main point of comparison with our
 304 method. The significant disadvantage of this approach is that the observation process (in this paper
 305 $\mathbf{y}_n = \mathbf{H}_n \mathbf{u}_n + \xi_n$) must be known at training time and kept the same at inference time (or kept the
 306 same in a distributional sense, as explained in the comparisons). However, in practice, the observation
 307 process for different physical systems can vary enormously as we measure different quantities such as
 308 moments, local averages, summary coefficients, have a variable number of observations, or vary the
 309 type and magnitude of noise etc. In contrast to this, GABI is independent of the observation process
 310 at training time and only requires this information at test time. Thus, GABI offers a train-once-use-
 311 everywhere type foundation model, hugely advantageous for practical/industry uptake of ML models.
 312 **Gaussian Process Regression.** For an inverse problem over fields, a natural choice of prior is a
 313 Gaussian process prior. As the observation process \mathbf{H}_o is linear, the classical Bayesian posterior for
 314 this problem is precisely a Gaussian process regression. We perform hyper-parameter optimization of
 315 this GP, which relates it to common usage of GPs in the context of ML. The GPs are defined directly
 316 on the graphs (Borovitskiy et al., 2021). **Bayesian NNs.** The problem of specifying informative
 317 priors over varying geometries persists and inherits the problems of direct maps discussed above.

318

4 NUMERICS

319

320

321

322

323

In this section we present numerical results for steady-state heat on rectangles, flow fields around
 324 airfoils, damped resonance and source localization on car bodies, and terrain flows. We compare
 325 our method to direct regression (Direct Map) using graph NNs, and Gaussian process regression
 326 (GPs) with Matérn kernels 1/2, 3/2, and radial basis function (RBF). In all experiments we report the
 327 wall-clock training time (Train) on Nvidia RTX 4090 GPUs (the terrain problem is multi-GPU), and

324

325

326

327

328

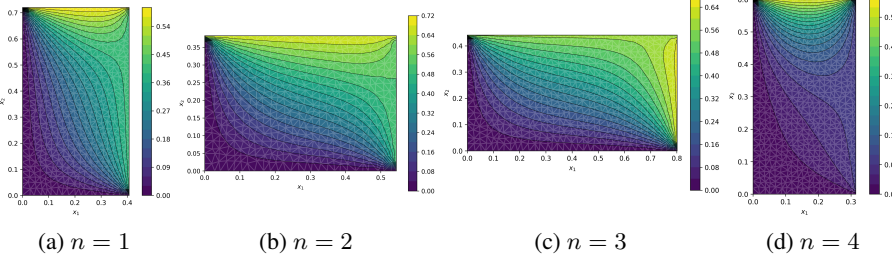
329

330

331

332

333

334 Figure 1: Four out of 1k geometries and solutions in dataset for the steady-state heat problem.
335
336

337

338

339

340

341

342

343

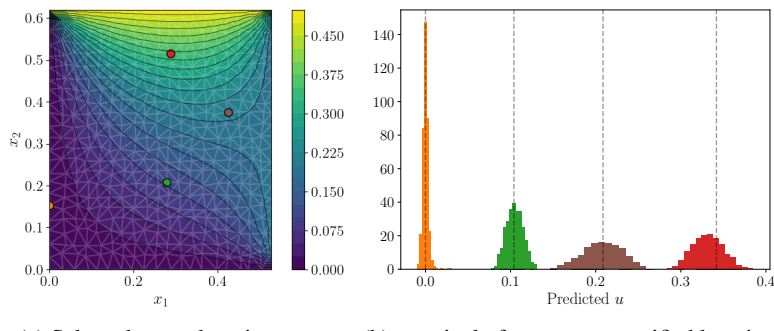
344

345

346

347

348

349 Figure 2: (a) Four selected query locations for the sampled predictive solutions given data, the full
350 field estimations are in Figure 6. (b) The corresponding histograms for the predictive posterior at
351 specified query locations; the dashed black line indicates the ground truth for each histogram.
352

353

354 the mean per-geometry prediction time (Pred.). We also note that in using ABC for sampling from
355 the posterior we do not need to compute the likelihood function. This may have strong advantages in
356 application where the observation process yields intractable likelihoods. In using GABI with MCMC,
357 as in the comparisons, we do compute the likelihood. In training the latent prior for GABI, the main
358 way we have of knowing if the autoencoder networks perform adequately for the inference task, is by
359 assessing the quality of reconstruction for a holdout set, as well as how close the embed holdout set
360 is to being Gaussian in the latent space, which assessed qualitatively and quantitatively.

360

361

4.1 RECTANGLES – STEADY-STATE HEAT

362

363 In this section, we study the homogeneous steady-state heat equation on rectangular domains with
364 varying width, height, and boundary conditions. Thus, for a given rectangle \mathcal{M}_n , boundary condition
365 h_n , any u_n satisfies the steady-state heat equation. We take $\mathcal{M}_n \subset \mathbb{R}^2$ to be $\mathcal{M}_n = \{x \in \mathbb{R}^2 : 0 < x_1 < l_n, 0 < x_2 < w_n\}$. The domain \mathcal{M}_n is defined by its length and width (l_n, w_n) drawn
366 from `uniform((0.1, 0.1), (1, 1))`; we specify h_n to be zero on the bottom and left side, and drawn
367 from `uniform((0.1, 0), (1, 1))` on the top and right. The solution to (9) depends on \mathcal{M}_n, h_n . We
368 generate 1k solutions to be in the training dataset. In Figure 1 we show example geometries and
369 solutions in the dataset. Once the model is trained on this data (the loss is shown in B.3) we select a
370 new observation vector and geometry $\mathcal{M}_o, \mathbf{y}_o$ and use ABC sampling as in Algorithm 1. Figure 2
371 (b) shows 4 coloured histograms corresponding to the marginal distribution of a decoded posterior
372 (based on 10 sparse observations in the vector \mathbf{y}_o) at the 4 queried locations on Figure 2 (a). As the
373 orange dot is close to a boundary with value 0 in the entire dataset (4 representative samples from the
374 1k geometry dataset can be seen in Figure 1), GABI present very small uncertainty in this area. As
375 we query points in areas where there is more variability of the solution in the dataset, GABI presents
376 wider uncertainty. In all cases the mean of the GABI posterior is very close to the ground truth
377 (vertical dashed line). This exemplifies the balance GABI strikes between sparse data and informative
378 data-driven priors. **Comparison – Known Noise.** In Table 1 we compare two sampling variants

378 Table 1: Comparison on Heat Equation in Rectangular Domain
379

380 Method	381 Field	382 MAE	383 % 1 std	384 % 2 std	385 Train	386 Pred.
2D Heat Rect. Domain						
GABI-ABC	(u)	$1.58 \cdot 10^{-2} \pm 1.36 \cdot 10^{-2}$	80.91%	95.59%	2.62hr	0.908s
GABI-NUTS	(u)	$1.11 \cdot 10^{-2} \pm 1.04 \cdot 10^{-2}$	66.66%	96.18%	”	410.31s
Direct Map	(u)	$1.25 \cdot 10^{-2} \pm 1.02 \cdot 10^{-2}$	—	—	1.47hr	0.0029s
GP (M 1/2)	(u)	$8.46 \cdot 10^{-2} \pm 4.18 \cdot 10^{-2}$	66.36%	89.45%	—	0.65s
GP (M 3/2)	(u)	$8.06 \cdot 10^{-2} \pm 4.85 \cdot 10^{-2}$	65.80%	87.22%	—	0.64s
GP (RBF)	(u)	$1.39 \cdot 10^{-1} \pm 6.66 \cdot 10^{-2}$	14.88%	29.36%	—	0.64s

389 Table 2: Comparison on Heat Equation in Rectangular Domain – Unknown Noise
390

392 Method	393 Field/QoI	394 MAE	395 % 1 std	396 % 2 std	397 Train	398 Pred.
GABI-ABC	(u)	$2.09 \cdot 10^{-2} \pm 1.62 \cdot 10^{-2}$	75.74%	94.76%	2.62hr	0.904s
Direct Map	(u)	$2.13 \cdot 10^{-2} \pm 2.27 \cdot 10^{-2}$	—	—	1.46hr	0.0030s
GP (M 1/2)	(u)	$7.73 \cdot 10^{-2} \pm 5.18 \cdot 10^{-2}$	64.87%	87.50%	—	0.615s
GP (M 3/2)	(u)	$7.56 \cdot 10^{-2} \pm 5.56 \cdot 10^{-2}$	51.58%	76.94%	—	0.686s
GP (RBF)	(u)	$1.40 \cdot 10^{-1} \pm 6.94 \cdot 10^{-2}$	18.03%	36.69%	—	0.694s
GABI-ABC	(σ)	$7.96 \cdot 10^{-1} \pm 5.74 \cdot 10^{-1}$	42.10%	69.11%	—	“ “
Direct Map	(σ)	—	—	—	—	—
GP (M 1/2)	(σ)	$1.08 \cdot 10^0 \pm 1.03 \cdot 10^0$	—	—	—	“ “
GP (M 3/2)	(σ)	$1.10 \cdot 10^0 \pm 1.47 \cdot 10^0$	—	—	—	“ “
GP (RBF)	(σ)	$2.01 \cdot 10^0 \pm 3.61 \cdot 10^0$	—	—	—	“ “

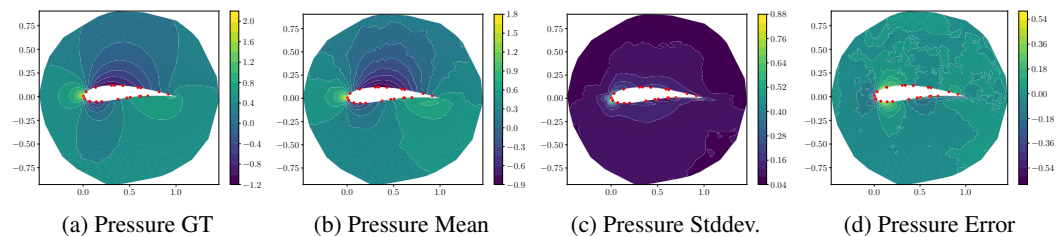
405 of GABI with a direct regression map as well as Gaussian Process Kriging with various kernels³;
406 M stands for Matérn. In this setup, we keep the number of observations at 10 randomly selected
407 locations and the noise standard deviation at 10^{-2} . **Comparison – Unknown Noise.** In Table 2
408 we test the noise estimation capabilities of GABI. We have the noise standard deviation be random
409 and drawn from a shifted log-normal distribution as $\sigma_n = \exp(\varepsilon_n - 4) + 10^{-3}; \varepsilon_n \sim \mathcal{N}(0, I)$. We
410 estimate the noise for each data \mathbf{y}_o with the GABI approach outlined in 2.3.

411
412

4.2 AIRFOILS – FLOW FIELD

413 In this section, we test the proposed methodology on the full field reconstruction of airflow around an
414 airfoil from a dataset of Reynolds averaged Navier-Stokes simulations. We use the setup described
415 in Duthé et al. (2025). Here, the geometric autoencoder is trained on the pressure and 2D velocity
416 field of 1k airfoil geometries with various inflow conditions. Once trained, the observation vector \mathbf{y}_o
417

418 ³GABI-NUTS was tested for 10^2 runs not 10^3 due to prediction runtime.
419



420
421
422
423
424
425
426
427
428
429
430
431 Figure 3: Comparison of ground truth (GT), inferred mean, error, and standard deviation for pressure (p). The red dots correspond to the observation location for the pressure. Full results including
432 reconstruction of vertical and horizontal velocity fields are in Figure 11

Table 3: Comparison on Airfoil

Method	Field	MAE	% 1 std	% 2 std	Train	Pred.
GABI-ABC	(p)	$6.92 \cdot 10^{-2} \pm 4.39 \cdot 10^{-2}$	78.77%	97.28%	8.61hr	34.76s
Direct Map	(p)	$5.35 \cdot 10^{-2} \pm 3.07 \cdot 10^{-2}$	—	—	4.68hr	0.0040s
GABI-ABC	(v_x)	$1.31 \cdot 10^{-1} \pm 3.62 \cdot 10^{-2}$	80.36%	97.28%	“ “	“ “
Direct Map	(v_x)	$9.30 \cdot 10^{-2} \pm 1.93 \cdot 10^{-2}$	—	—	“ “	“ “
GABI-ABC	(v_y)	$3.94 \cdot 10^{-2} \pm 2.20 \cdot 10^{-2}$	75.87%	96.08%	“ “	“ “
Direct Map	(v_y)	$3.24 \cdot 10^{-2} \pm 1.12 \cdot 10^{-2}$	—	—	“ “	“ “

Table 4: Comparison on Car Resonance – Full Field Reconstruction and Source Localization

Method	Field	MAE	% 1 std	% 2 std	Train	Pred.
GABI-ABC	(u)	$2.32 \cdot 10^{-1} \pm 7.21 \cdot 10^{-2}$	75.48%	96.88%	2.29hr	18.14s
Direct Map	(u)	$6.03 \cdot 10^{-1} \pm 1.46 \cdot 10^{-1}$	—	—	1.22hr	0.0032s
GABI-ABC	(f)	$2.26 \cdot 10^{-3} \pm 4.36 \cdot 10^{-4}$	80.55%	97.49%	“ “	“ “
Direct Map	(f)	$2.46 \cdot 10^{-1} \pm 8.76 \cdot 10^{-2}$	—	—	“ “	“ “

is taken to be noisy pressure observations at a small number of nodes on the surface of the airfoil, emulating a physical scenario when such pressure sensors may be attached to a wing/blade. The Bayesian inversion task is to reconstruct the pressure and velocity field around the airfoil, a task far too ill-posed without a highly informative prior. To compile the results in Table 3 we test GABI-ABC against the Direct Map with the same architecture type – we randomize the number of observation locations to be drawn between 5 and 50 observations with probability inversely proportional to the number of observation locations. For the supervised Direct Map approach the distribution of the number of observation must be known at train time, this is not the case for GABI who’s training is independent of the observation process. Figure 3 shows a select number of results. For a discussion on out-of-distribution inference we refer the reader to Appendix B.4.2.

4.3 CAR BODY – ACOUSTIC VIBRATION AND SOURCE LOCALIZATION

Here, we study an acoustic resonance problem with a source localization task. We have a collection of car body geometries which undergo damped vibration due to a localized Gaussian bump forcing present in the first 1/5 of the vehicle (where the engine is), the inversion task is to reconstruct the full field acoustic vibration amplitude, u , as well as reconstruct the full field forcing, f , on the surface of the vehicle from a small number of sparse noisy measurements of the vibration amplitude, we do not observe the forcing field. The car geometries are taken from (Umetani & Bickel, 2018). We train the model on 500 car geometries, the number of observation location is randomized as in Section 4.2. The numerical results are in Table 4 and we show a reconstruction result in Figure 4.

4.4 TERRAIN – FLOW FIELD

To demonstrate the scalability of our approach, we apply it to the reconstruction of flow fields over complex terrain. Here, we use a large dataset (127GB) of more than 5k RANS simulations, produced by Achermann et al. (2024). From the original 64^3 grids, we extract 8-voxel-thick, terrain-conforming layers, resulting in $64 \times 64 \times 8$ subdomains. Each subdomain is then converted into a graph, where voxels become nodes connected to their adjacent neighbors. We scale both the training and the inference methods with multi-GPU pipelines. Using four RTX4090 GPUs, training takes 52hr, while inference takes 480s. Figure 5 shows the GABI-ABC pressure and velocity results.

5 CONCLUSION

We propose a methodology for learning highly informative priors for solving Bayesian inverse problems across varying geometries. The scheme is realized through a geometric autoencoder which learns informative latent representations allowing for sharing of information across geometries. Once

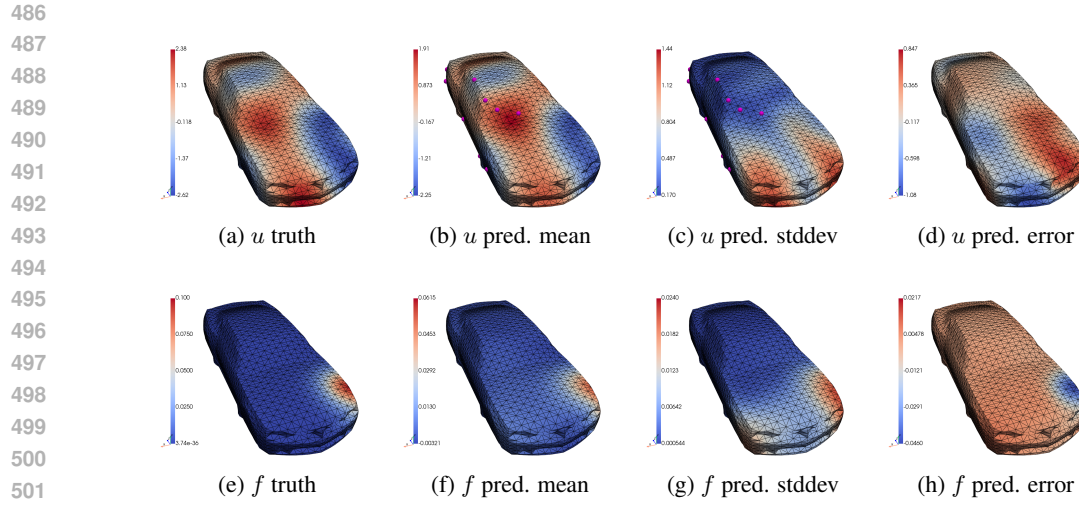


Figure 4: Ground truth, inferred mean, stddev., and error for amplitude u , and forcing f . In magenta are the observation locations.

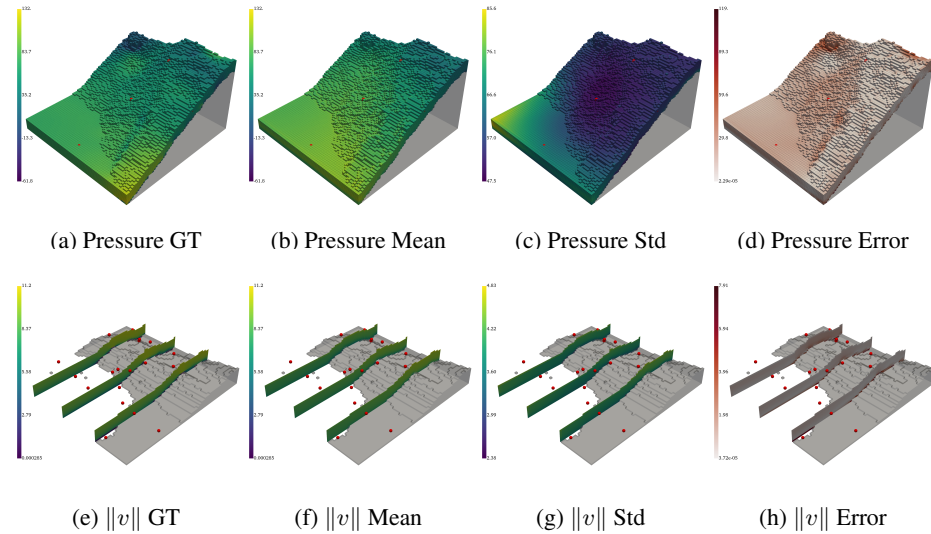


Figure 5: Ground truth, inferred mean, error, and standard deviation for pressure and the magnitude of the velocity vector, ($\|v\|$) across two terrains. The red dots correspond to the observation locations.

trained this foundation model can be used with any observation process to perform Bayesian full field reconstruction over new geometries. A creative use of ABC sampling leads to an efficient GPU implementation. The method achieves similar predictive accuracy to supervised direct map methods, all while outputting a full Bayesian posterior over the fields of interest and being far more flexible due to the model being independent from the observation process. The method is tested on a wide range of physical setups and geometries.

REFERENCES

Florian Achermann, Thomas Stastny, Bogdan Danciu, Andrey Kolobov, Jen Jen Chung, Roland Siegwart, and Nicholas Lawrance. Windseer: real-time volumetric wind prediction over complex terrain aboard a small uncrewed aerial vehicle. *Nature Communications*, 15(1):3507, 2024.

540 Kingma DP Ba J Adam et al. A method for stochastic optimization. *arXiv preprint arXiv:1412.6980*,
 541 1412(6), 2014.

542

543 Jonas Adler and Ozan Öktem. Solving ill-posed inverse problems using iterative deep neural networks.
 544 *Inverse Problems*, 33(12):124007, 2017.

545

546 Jonas Adler, Sebastian Lunz, Olivier Verdier, Carola-Bibiane Schönlieb, and Ozan Öktem. Task
 547 adapted reconstruction for inverse problems. *Inverse Problems*, 38(7):075006, 2022.

548

549 O Deniz Akyildiz, Mark Girolami, Andrew M Stuart, and Arnaud Vadeboncoeur. Efficient prior
 550 calibration from indirect data. *SIAM Journal on Scientific Computing*, 47(4):C932–C958, 2025.

551

552 Lynton Ardizzone, Jakob Kruse, Sebastian Wirkert, Daniel Rahner, Eric W Pellegrini, Ralf S Klessen,
 553 Lena Maier-Hein, Carsten Rother, and Ullrich Köthe. Analyzing inverse problems with invertible
 554 neural networks. *arXiv preprint arXiv:1808.04730*, 2018.

555

556 Simon Arridge, Peter Maass, Ozan Öktem, and Carola-Bibiane Schönlieb. Solving inverse problems
 557 using data-driven models. *Acta Numerica*, 28:1–174, 2019.

558

559 Ricardo Baptista, Bamdad Hosseini, Nikola B Kovachki, and Youssef M Marzouk. Conditional
 560 sampling with monotone gans: From generative models to likelihood-free inference. *SIAM/ASA
 Journal on Uncertainty Quantification*, 12(3):868–900, 2024.

561

562 Vladimir Igorevich Bogachev and Maria Aparecida Soares Ruas. *Measure theory*, volume 1. Springer,
 563 2007.

564

565 Viacheslav Borovitskiy, Iskander Azangulov, Alexander Terenin, Peter Mostowsky, Marc Deisenroth,
 566 and Nicolas Durrande. Matérn gaussian processes on graphs. In *International Conference on
 567 Artificial Intelligence and Statistics*, pp. 2593–2601. PMLR, 2021.

568

569 Benjamin Boys, Mark Girolami, Jakiw Pidstrigach, Sebastian Reich, Alan Mosca, and O Deniz
 570 Akyildiz. Tweedie moment projected diffusions for inverse problems. *Transactions of Machine
 571 Learning Research (TMLR)*, 2024.

572

573 Michael M Bronstein, Joan Bruna, Taco Cohen, and Petar Veličković. Geometric deep learning:
 574 Grids, groups, graphs, geodesics, and gauges. *arXiv preprint arXiv:2104.13478*, 2021.

575

576 Daniela Calvetti and Lothar Reichel. Tikhonov regularization of large linear problems. *BIT Numerical
 577 Mathematics*, 43(2):263–283, 2003.

578

579 Shuhao Cao. Choose a transformer: Fourier or galerkin. *Advances in neural information processing
 580 systems*, 34:24924–24940, 2021.

581

582 Sören Dittmer, Tobias Kluth, Peter Maass, and Daniel Otero Baguer. Regularization by architecture:
 583 A deep prior approach for inverse problems. *Journal of Mathematical Imaging and Vision*, 62(3):
 584 456–470, 2020.

585

586 Gregory Duthé, Imad Abdallah, and Eleni Chatzi. Graph transformers for inverse physics: recon-
 587 structing flows around arbitrary 2d airfoils. *arXiv preprint arXiv:2501.17081*, 2025.

588

589 Berthy T Feng, Jamie Smith, Michael Rubinstein, Huiwen Chang, Katherine L Bouman, and
 590 William T Freeman. Score-based diffusion models as principled priors for inverse imaging.
 591 In *Proceedings of the IEEE/CVF International Conference on Computer Vision*, pp. 10520–10531,
 592 2023.

593

594 Han Gao, Matthew J Zahr, and Jian-Xun Wang. Physics-informed graph neural galerkin networks: A
 595 unified framework for solving pde-governed forward and inverse problems. *Computer Methods in
 596 Applied Mechanics and Engineering*, 390:114502, 2022.

597

598 Nicolas Garcia Trillos and Daniel Sanz-Alonso. Continuum limits of posteriors in graph bayesian
 599 inverse problems. *SIAM Journal on Mathematical Analysis*, 50(4):4020–4040, 2018.

594 Hwan Goh, Sheroze Sheriffdeen, Jonathan Wittmer, and Tan Bui-Thanh. Solving bayesian inverse
 595 problems via variational autoencoders. In Joan Bruna, Jan Hesthaven, and Lenka Zdeborova (eds.),
 596 *Proceedings of the 2nd Mathematical and Scientific Machine Learning Conference*, volume 145
 597 of *Proceedings of Machine Learning Research*, pp. 386–425. PMLR, 16–19 Aug 2022. URL
 598 <https://proceedings.mlr.press/v145/goh22a.html>.

599 Arthur Gretton, Karsten M. Borgwardt, Malte J. Rasch, Bernhard Schölkopf, and Alexander Smola.
 600 A kernel two-sample test. *Journal of Machine Learning Research*, 13(25):723–773, 2012. URL
 601 <http://jmlr.org/papers/v13/gretton12a.html>.

602 Matthew D Hoffman, Andrew Gelman, et al. The no-u-turn sampler: adaptively setting path lengths
 603 in hamiltonian monte carlo. *J. Mach. Learn. Res.*, 15(1):1593–1623, 2014.

604 Jari P Kaipio and Erkki Somersalo. *Statistical and computational inverse problems*. Springer, 2005.

605 Sebastian Kaltenbach, Paris Perdikaris, and Phaedon-Stelios Koutsourelakis. Semi-supervised
 606 invertible neural operators for bayesian inverse problems. *Computational Mechanics*, 72(3):
 607 451–470, 2023.

608 Thomas N Kipf and Max Welling. Variational graph auto-encoders. *arXiv preprint arXiv:1611.07308*,
 609 2016.

610 TN Kipf. Semi-supervised classification with graph convolutional networks. *arXiv preprint
 611 arXiv:1609.02907*, 2016.

612 Soheil Kolouri, Phillip E Pope, Charles E Martin, and Gustavo K Rohde. Sliced wasserstein auto-
 613 encoders. In *ICLR (Poster)*, 2019.

614 Eric Laloy, Romain Hérault, John Lee, Diederik Jacques, and Niklas Linde. Inversion using a
 615 new low-dimensional representation of complex binary geological media based on a deep neural
 616 network. *Advances in water resources*, 110:387–405, 2017.

617 Eric Laloy, Romain Hérault, Diederik Jacques, and Niklas Linde. Training-image based geostatistical
 618 inversion using a spatial generative adversarial neural network. *Water Resources Research*, 54(1):
 619 381–406, 2018.

620 Samuel Lanthaler, Zongyi Li, and Andrew M Stuart. Nonlocality and nonlinearity implies universality
 621 in operator learning. URL <https://arxiv.org/abs/2304.13221>, 2024.

622 Guohao Li, Chenxin Xiong, Ali Thabet, and Bernard Ghanem. Deepergcn: All you need to train
 623 deeper gcns. *arXiv preprint arXiv:2006.07739*, 2020.

624 Chein-Shan Liu, Chih-Wen Chang, and Chia-Cheng Tsai. Numerical simulations of complex
 625 helmholtz equations using two-block splitting iterative schemes with optimal values of parameters.
 626 *AppliedMath*, 4(4):1256–1277, 2024.

627 Jenny Liu, Aviral Kumar, Jimmy Ba, Jamie Kiros, and Kevin Swersky. Graph normalizing flows.
 628 *Advances in Neural Information Processing Systems*, 32, 2019.

629 Ilya Loshchilov and Frank Hutter. Decoupled weight decay regularization. *arXiv preprint
 630 arXiv:1711.05101*, 2017.

631 Xuhui Meng, Liu Yang, Zhiping Mao, José del Águila Ferrandis, and George Em Karniadakis.
 632 Learning functional priors and posteriors from data and physics. *Journal of Computational Physics*,
 633 457:111073, 2022.

634 Peter Mostowsky, Vincent Dutordoir, Iskander Azangulov, Noémie Jaquier, Michael John Hutchinson,
 635 Aditya Ravuri, Leonel Rozo, Alexander Terenin, and Viacheslav Borovitskiy. The geometrickernels
 636 package: Heat and matérn kernels for geometric learning on manifolds, meshes, and graphs.
 637 *arXiv:2407.08086*, 2024.

638 Charilaos Mylonas, Imad Abdallah, and Eleni Chatzi. Relational vae: A continuous latent variable
 639 model for graph structured data. *arXiv preprint arXiv:2106.16049*, 2021.

648 Philipp Nazari, Sebastian Damrich, and Fred A Hamprecht. Geometric autoencoders—what you see is
 649 what you decode. *arXiv preprint arXiv:2306.17638*, 2023.
 650

651 Dhruv V Patel and Assad A Oberai. Gan-based priors for quantifying uncertainty in supervised
 652 learning. *SIAM/ASA Journal on Uncertainty Quantification*, 9(3):1314–1343, 2021.
 653

654 Dhruv V Patel, Deep Ray, and Assad A Oberai. Solution of physics-based bayesian inverse problems
 655 with deep generative priors. *Computer Methods in Applied Mechanics and Engineering*, 400:
 656 115428, 2022.
 657

658 Tobias Pfaff, Meire Fortunato, Alvaro Sanchez-Gonzalez, and Peter Battaglia. Learning mesh-based
 659 simulation with graph networks. In *International conference on learning representations*, 2020.
 660

661 Jan Povala, Ieva Kazlauskaitė, Eky Febrianto, Fehmi Cirak, and Mark Girolami. Variational bayesian
 662 approximation of inverse problems using sparse precision matrices. *Computer Methods in Applied
 663 Mechanics and Engineering*, 393:114712, 2022.
 664

665 Maziar Raissi, Paris Perdikaris, and George E Karniadakis. Physics-informed neural networks: A
 666 deep learning framework for solving forward and inverse problems involving nonlinear partial
 667 differential equations. *Journal of Computational physics*, 378:686–707, 2019.
 668

669 Maximilian Rixner and Phaedon-Stelios Koutsourelakis. A probabilistic generative model for semi-
 670 supervised training of coarse-grained surrogates and enforcing physical constraints through virtual
 671 observables. *Journal of Computational Physics*, 434:110218, 2021.
 672

673 Sungyong Seo and Yan Liu. Differentiable physics-informed graph networks. *arXiv preprint
 674 arXiv:1902.02950*, 2019.
 675

676 Ravid Shwartz-Ziv, Micah Goldblum, Hossein Souri, Sanyam Kapoor, Chen Zhu, Yann LeCun, and
 677 Andrew G Wilson. Pre-train your loss: Easy bayesian transfer learning with informative priors.
 678 *Advances in Neural Information Processing Systems*, 35:27706–27715, 2022.
 679

680 Kihyuk Sohn, Honglak Lee, and Xinchen Yan. Learning structured output representation using deep
 681 conditional generative models. *Advances in neural information processing systems*, 28, 2015.
 682

683 Andrew M Stuart. Inverse problems: a bayesian perspective. *Acta numerica*, 19:451–559, 2010.
 684

685 Ilya Tolstikhin, Olivier Bousquet, Sylvain Gelly, and Bernhard Schoelkopf. Wasserstein auto-encoders.
 686 In *International Conference on Learning Representations*, 2018.
 687

688 Gabriel Turinici. Radon–sobolev variational auto-encoders. *Neural Networks*, 141:294–305,
 689 2021. ISSN 0893-6080. doi:<https://doi.org/10.1016/j.neunet.2021.04.018>. URL <https://www.sciencedirect.com/science/article/pii/S0893608021001556>.
 690

691 Nobuyuki Umetani and Bernd Bickel. Learning three-dimensional flow for interactive aerodynamic
 692 design. *ACM Transactions on Graphics (TOG)*, 37(4):1–10, 2018.
 693

694 Arnaud Vadeboncoeur, Ömer Deniz Akyıldız, Ieva Kazlauskaitė, Mark Girolami, and Fehmi Cirak.
 695 Fully probabilistic deep models for forward and inverse problems in parametric pdes. *Journal of
 696 Computational Physics*, 491:112369, 2023.
 697

698 Mario Lino Valencia, Tobias Pfaff, and Nils Thuerey. Learning distributions of complex fluid
 699 simulations with diffusion graph networks. In *The Thirteenth International Conference on Learning
 700 Representations*, 2025.
 701

702 Nils Wandel, Michael Weinmann, and Reinhard Klein. Learning incompressible fluid dynamics from
 703 scratch—towards fast, differentiable fluid models that generalize. *arXiv preprint arXiv:2006.08762*,
 704 2020.
 705

706 Lingfei Wu, Peng Cui, Jian Pei, Liang Zhao, and Xiaojie Guo. Graph neural networks: foundation,
 707 frontiers and applications. In *Proceedings of the 28th ACM SIGKDD conference on knowledge
 708 discovery and data mining*, pp. 4840–4841, 2022.

702 Chen Xu, Ba Trung Cao, Yong Yuan, and Günther Meschke. Transfer learning based physics-
 703 informed neural networks for solving inverse problems in engineering structures under different
 704 loading scenarios. *Computer Methods in Applied Mechanics and Engineering*, 405:115852, 2023.

705 Shengjia Zhao, Jiaming Song, and Stefano Ermon. Infovae: Balancing learning and inference
 706 in variational autoencoders. In *Proceedings of the aaai conference on artificial intelligence*,
 707 volume 33, pp. 5885–5892, 2019.

710 A PROOFS

712 A.1 PROOF OF LEMMA 2.1

714 *Proof.* We remember

$$715 \quad Z(y) = \int_{\mathcal{U}} \exp(-\Phi(u; y)) d\mathbb{P}_u, \quad \mathbb{P}_u := g_{\#}\mathbb{P}_z.$$

718 Thus, assuming the relevant measurabilities,

$$719 \quad Z(y) = \int_{\mathcal{U}} \exp(-\Phi(u; y)) d(g_{\#}\mathbb{P}_z) \\ 720 \quad = \int_{\mathcal{Z}} \exp(-\Phi(g(u); y)) d\mathbb{P}_z,$$

723 where the second equality is given by Theorem 3.6.1 in Bogachev & Ruas (2007). Applying the same
 724 equality, $\forall A \in \mathcal{F}$,

$$726 \quad \mathbb{P}_{u|y}(A) = \frac{1}{Z(y)} \int_A \exp(-\Phi(u; y)) d(g_{\#}\mathbb{P}_z) \\ 727 \quad = \frac{1}{Z(y)} \int_{\mathcal{U}} \mathbb{1}_A(u) \exp(-\Phi(u; y)) d(g_{\#}\mathbb{P}_z) \\ 728 \quad = \frac{1}{Z(y)} \int_{\mathcal{Z}} \mathbb{1}_A(g(z)) \exp(-\Phi(g(z); y)) d\mathbb{P}_z \\ 729 \quad = \frac{1}{Z(y)} \int_{\mathcal{Z}} \mathbb{1}_{g^{-1}(A)}(z) \exp(-\Phi(g(z); y)) d\mathbb{P}_z \\ 730 \quad = \frac{1}{Z(y)} \int_{g^{-1}(A)} \exp(-\Phi(g(z); y)) d\mathbb{P}_z \\ 731 \quad = \mathbb{P}_{z|y}(g^{-1}(A)) \\ 732 \quad = (g_{\#}\mathbb{P}_{z|y})(A),$$

739 where $\mathbb{1}_A$ is the indicator function. Hence, $\mathbb{P}_{u|y} = g_{\#}\mathbb{P}_{z|y}$. \square

742 A.2 PROOF OF THEOREM 2.2

743 *Proof.* Using Lemma 2.1, replacing g with D_o^ψ , identifying z, u, y with $\mathbf{z}, \mathbf{u}_o, \mathbf{y}_o$, we obtain the
 744 desired posterior. \square

746 A.3 PROOF OF COROLLARY 2.3

748 *Proof.* This follows directly from Lemma 2.1 and Theorem 2.2 by identifying z with (\mathbf{z}, σ_o) , \mathbb{P}_z with
 749 $(\mathbb{P}_{\mathbf{z}} \otimes \mathbb{P}_{\sigma_o})$, g with $(D_o^\psi \otimes \text{Id.})$, changing to potential function to $\Phi(\mathbf{u}_o, \sigma_o; \mathbf{y}_o) = \frac{1}{2\sigma_o^2} \|\mathbf{y}_o - \mathbf{H}_o \mathbf{u}_o\|_2^2$,
 750 and finally noting $\text{Id.}_{\#}\mathbb{P}_{\sigma_o} = \mathbb{P}_{\sigma_o}$. \square

752 B ADDITIONAL NUMERICAL RESULTS AND DETAILS

753 The proposed methodology is architecture agnostic, however for an architecture to be appropriate for
 754 the task we require a few particular qualities:

- **Geometry aware architecture and data-structure.** As the main premise of this work is to share information about physical fields which depend on the geometry of the problem to which they relate, it is essential that the data-structure reflect this geometric information, and that the neural networks used be effective at processing this information.
- **Mapping to and from fixed-dimensional vectors.** This framework relies on learning latent representations between solution to PDEs and the geometries on which these are defined. Hence, one needs to map to and from fixed dimensional latent spaces from arbitrary geometries.
- **Non-locality.** All physical processes in this paper behave in non-local ways, the solution field at one point in the domain affects the solution at all other points in the domain. Hence, when encoding solution fields for a given geometry, the encoder/decoder should reflect this non-locality.

We use three architectures, a Graph Convolutional Network (explained in B.1), a Generalized Aggregation Network (explained in B.2), and a transformer (explained and tested in B.3.3).

B.1 GRAPH CONVOLUTIONAL NETWORK

We use graph convolutional layers (Kipf, 2016) in the examples heat on rectangles, RANS around airfoil, Helmholtz on car. To induce non-locality of mappings across channels, c , at each layer we set $\text{GCN}_l : M_n \times \mathbb{R}^{2c} \rightarrow M_n \times \mathbb{R}^c$ and the output is concatenated with a graph level channel wise average which is expanded to populate each node of the graph. The edge attributes are the distance between nodes. The input node values always contain the node coordinates, and, for the encoder, also the data solution at the node.

In GABI: In the encoder E^θ we map attributed graphs to latent vectors of fixed dimensions. The decoder maps a pairing between a latent variable and a graph and populates the node attributes on the input graph. Hence the last layer in a channel wise averaging across the graph and the channel dimension is taken to be the latent dimension. The decoder D^ψ takes as argument a graph where the node attributes are only the coordinates, hence only contains geometric information, and we expand the latent sample \mathbf{z} to decode to populate all nodes with channel dimension equal the latent dimension.

In Direct Map: For the direct map method we use the same GCN layers as explained above. However now we must map observation vectors \mathbf{y}_n and geometry M_n directly to the solution on the geometry, \mathbf{u}_n . To do this, we make the input graph node attributes the coordinates of the nodes as per the previous section, the observed nodal values \mathbf{y}_n (where other values are 0), and a one-hot encoding indicates where this node is observed or not.

GP Regression: We use a graph Matérn Gaussian process (Mostowsky et al., 2024) with maximum marginal likelihood estimation of the hyperparameters.

The rectangle, airfoil, and car examples are run on a single RTX4090 GPU. The terrain example is run in a multi-GPU manner.

B.2 GENERALIZED AGGREGATION NETWORK (GEN)

For the graph-based autoencoder applied to the flow over complex terrain, we replace standard GCN layers with Generalized Aggregation Network (GEN) layers (Li et al., 2020). This change allows us to add more complex geometrical information to the edge features (relative coordinates, similarly to (Pfaff et al., 2020)), as GEN layers, unlike GCNs, can process multidimensional edge features. This message-passing formulation also uses a softmax-based message aggregation scheme, which allows the model to dynamically weigh the importance of messages from neighboring nodes. Importantly, we maintain the same non-local pooling operation for each layer as for the GCN-based approach.

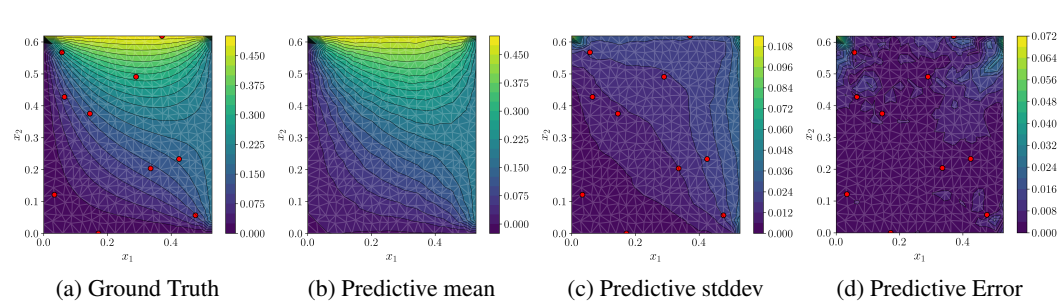


Figure 6: For the heat setup, we overlay in red the observation locations. (a) ground truth (b) decoded mode of predictive posterior. (c) empirical standard deviation of decoded posterior samples. (d) error between decoded mode and ground truth.

Table 5: Comparison of Graph Convolutional Network (GCN) and Transformer (T) architectures: Heat Equation in Rectangular Domain

Method	Field	MAE	% 1 std	% 2 std	Train	Pred.
T: GABI-ABC	(u)	$1.19 \cdot 10^{-2} \pm 8.65 \cdot 10^{-3}$	82.97%	97.97%	18.89hr	10.17s
T: Direct Map	(u)	$1.01 \cdot 10^{-2} \pm 6.69 \cdot 10^{-3}$	—	—	11.00hr	0.0063s
GCN: GABI-ABC	(u)	$1.58 \cdot 10^{-2} \pm 1.36 \cdot 10^{-2}$	80.91%	95.59%	2.62hr	0.908s
GCN: Direct Map	(u)	$1.25 \cdot 10^{-2} \pm 1.02 \cdot 10^{-2}$	—	—	1.47hr	0.0029s

B.3 HEAT

In this section, we add numerical information and results for the steady-state heat problem. The equation used to generate the dataset is

$$\Delta u(x) = 0, \quad x \in \mathcal{M}_n, \quad (9a)$$

$$u(x) = h_n(x), \quad x \in \partial \mathcal{M}_n. \quad (9b)$$

where h_n is described in Section 4.1. We use a finite element solver over an unstructured triangular mesh to solve the systems to be in the dataset.

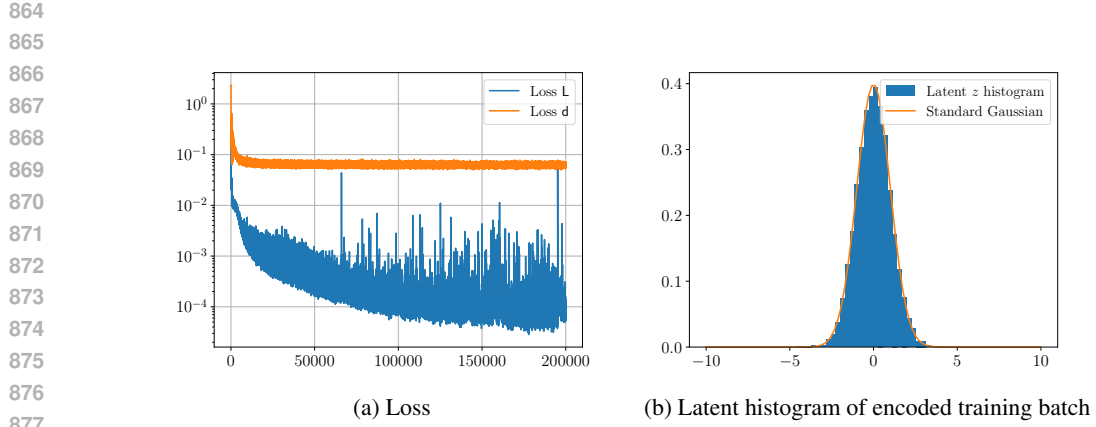
B.3.1 IMPLEMENTATION DETAILS

Train: We use a 6-layer GCN as described in B.1 with a 100 dimensional channel space and latent space. We use 1k training geometries and train the model for 20k iterations using the Adam optimizer (Adam et al., 2014) with a learning rate of 10^{-3} . We use a training batch size of 100.

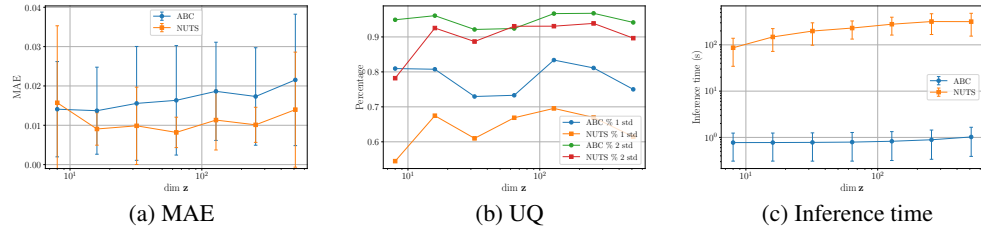
Pred: Once trained, at inference time, in GABI-ABC we decode 10k samples in 100 batches of 100 samples. We keep 100 samples as being drawn from the posterior.

B.3.2 ADDITIONAL RESULTS

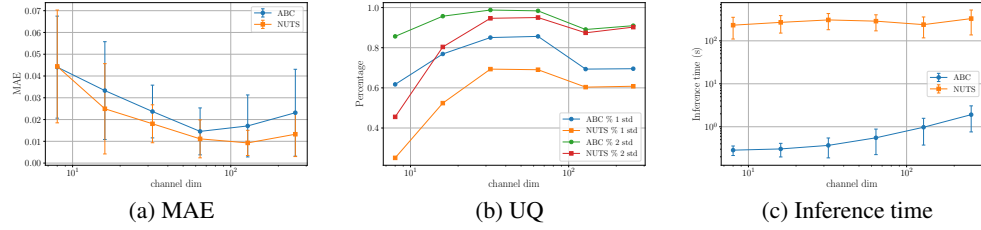
In Figure 6 we show the results of inference with GABI-ABC on for the full field reconstructing based on the small number of sparse noisy observations in red. In Figure 7 we show the two terms in the loss for training the GABI autoencoder as well as a histogram of the encoded data batch overlaid with the 1D standard normal distribution. We then test the performance of ABC sampling vs NUTS sampling as we vary the dimension of the latent space for the heat inversion task. The MAE, quality of UQ, and inference times are shown in Figure 8. In Figure 9 we perform an ablation study on the size of the channel space of the graph autoencoder for a fixed latent dimension of 100 for Bayesian inversion with both ABC and MCMC sampling. From this, we can assess the importance of network size for accuracy and efficiency.



878
879
Figure 7: (a) Loss functions during training – the total loss is the sum of these. (b) histogram of the
880 latent p_z^θ across all dimensions after training.



896
897
898
899
900
901
902
903
Figure 8: Sampling schemes on the same autoencoder model with the same channel space and different
904 latent dimensions. We compare (a) mean absolute predictive error, (b) uncertainty quantification
905 under a Gaussian assumption, (c) sampling time.



918
919
920
921
922
923
924
925
926
927
928
929
930
Figure 9: Sampling schemes on the same autoencoder model with different channel space dimensions
931 and same the latent dimension (fixed at 100). We compare (a) mean absolute predictive error, (b)
932 uncertainty quantification under a Gaussian assumption, (c) sampling time.

B.3.3 TRANSFORMER GABI

933 As our framework is architecture-agnostic, we also test a Transformer-based variant. Transformers
934 can function as neural operators (Cao, 2021), achieving non-locality through attention mechanisms.
935 Unlike the graph-based approach, this variant treats the input as an unordered point set with coordinates,
936 without exploiting the underlying graph structure. We implement 4-layer Transformers for the
937 encoding and decoding networks with 64-dimensional embeddings and 8 attention heads per layer,
938 resulting in a comparable number of trainable parameters: $\sim 200k$ for GABI and $\sim 100k$ for the
939 direct map. As shown in Table 5, we obtain similar results to the GCN-based approach (with the
940 same training setup), but much slower training and prediction times, which can be attributed to the
941 dense self-attention operations of the Transformer layers.

918 B.4 AIRFOIL
919920 B.4.1 IMPLEMENTATION DETAILS
921922 **Train:** We use an 8-layer GCN as described in B.1 with a 100 dimensional channel space and
923 latent space. We use 1k training geometries and train the model for 10k iterations using the Adam
924 optimizer (Adam et al., 2014) with a learning rate of 10^{-3} with an exponential decay learning rate
925 with decay rate 0.999. We use a training batch size of 100.926 **Pred:** Once trained, at inference time, in GABI-ABC we decode 50k samples in 100 batches of 500
927 samples. We keep 100 samples as being drawn from the posterior.928 B.4.2 ADDITIONAL RESULTS
929930 In Figure 10 we show four samples from the full field dataset. In Figure 11 we show a complete
931 example of results from the airfoil inversion task. We only measure the noisy pressure along the
932 surface of the airfoil on the red scatter points and infer from this the full pressure field and 2D velocity
933 field. In Figure 12 we show four random samples drawn from the generative prior model for a given
934 geometry, demonstrating the physical coherence and diversity of the prior.935 We now test the behaviour of GABI-ABC inference on 10 out-of-distribution airfoil geometries.
936 In Figure 13 we plot a histogram of the density of the training dataset geometries and a selection
937 of out of distribution airfoils. The x-axis shows the Mahalanobis distance (empirical covariance
938 weighted distance of a point to the mean) between these shapes and the training dataset. The distance
939 in geometry is computed using 9 summary statistics regarding airfoil thickness, camber, trailing-edge
940 thickness, etc. We report the MAE and percentage of the ground truth between one and two standard
941 deviations of the predictive posterior for pressure (reconstructed with GABI using 20 observations).
942 These tests suggest that the GABI framework has some mild, but limited, robustness to prediction for
943 outliers. Eventually, the miss-specification of the prior for such out-of-distribution geometries may
944 lead to unreliable inference.945 B.5 CAR
946947 For the car resonance and source localization problem we create the dataset by solving the damped
948 Helmholtz equation (Liu et al., 2024) on a closed manifold
949

950
$$(\Delta_{\mathcal{M}_n} - \kappa + i\gamma\kappa) u(x) = f(x), \quad x \in \mathcal{M}_n. \quad (10)$$

951 where $i = \sqrt{-1}$, $\kappa = 500$ is a wave speed parameter, and $\gamma = 0.2$ is a damping parameter.
952953 B.5.1 IMPLEMENTATION DETAILS
954955 **Train:** We use an 6-layer GCN as described in B.1 with a 100 dimensional channel space and latent
956 space. We use 500 training geometries and train the model for 10k iterations using the AdamW
957 optimizer (Loshchilov & Hutter, 2017) with an initial learning rate of 10^{-3} with and cosine decay
958 learning minimum rate of 10^{-5} . We use a training batch size of 100.959 **Pred:** Once trained, at inference time, in GABI-ABC we decode 50k samples in 100 batches of 500
960 samples. We keep 100 samples as being drawn from the posterior.
961962 B.5.2 ADDITIONAL RESULTS
963964 In Figure 14 we show some example geometries along with the forcing function to and resonance
965 field to reconstruct. In Figure 15 we show 3 random draws from the prior for a given geometry to
966 show the diversity of solutions and forcing fields.
967968 B.6 TERRAIN
969970 B.6.1 IMPLEMENTATION DETAILS
971972 **Train:** For both the encoding and decoding layers of the autoencoder we use an encode-process-
973 decode backbone (Pfaff et al., 2020; Duthé et al., 2025), where each processing block is composed

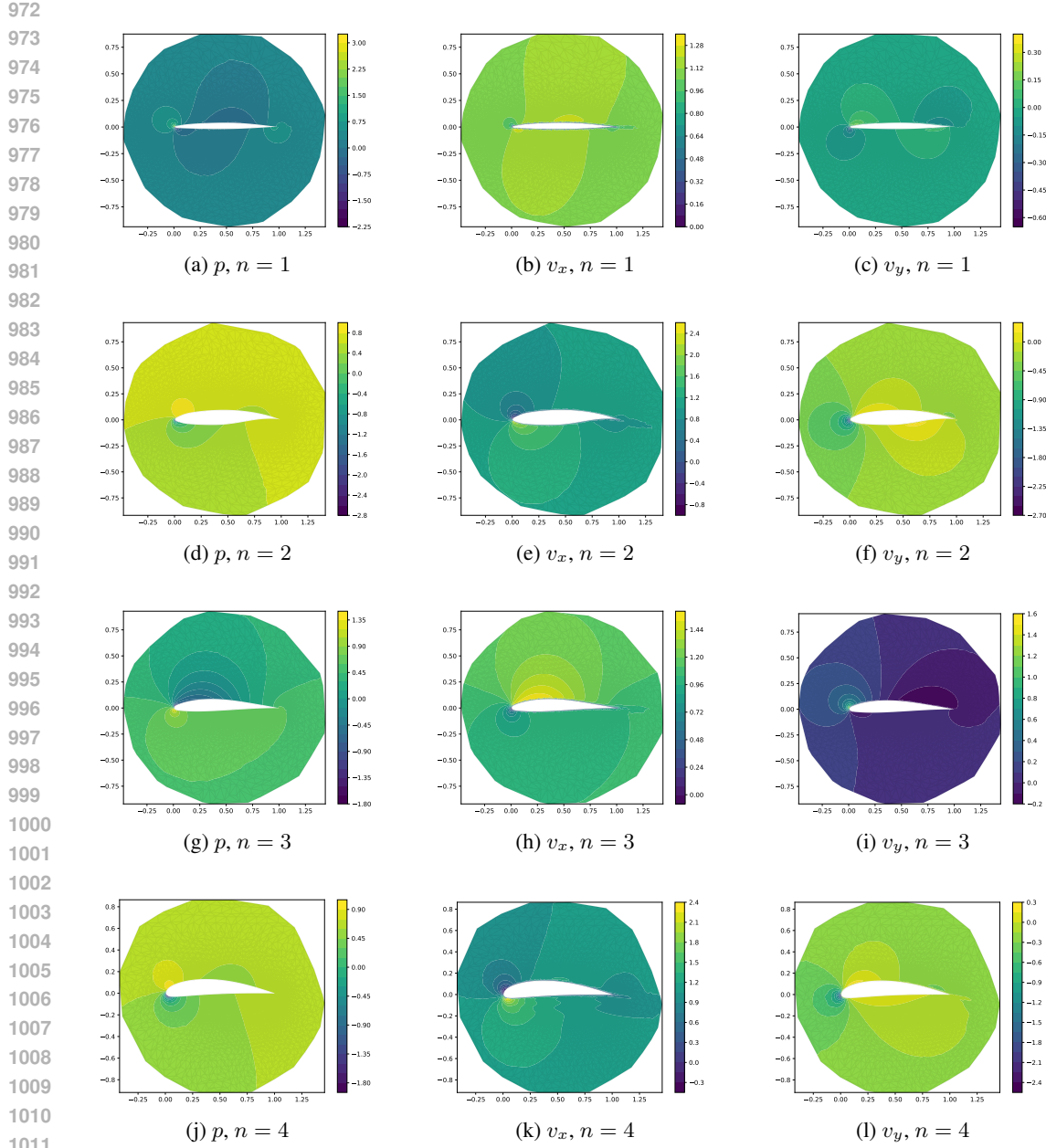


Figure 10: Four samples from the Airfoil dataset for pressure, horizontal and vertical velocity fields.

of a 6-layer GEN-based GNN. Both edge and node features are projected to latent vectors with 64 dimensions. We train the model for around 300 epochs using the Adam optimizer with an exponential learning rate decay (initial learning rate of 10^{-3} , decay exponent of 0.99). This takes around 52 hours on our distributed training pipeline across four RTX4090 GPUs with an overall batch size of 20 graphs.

We process the training samples from Achermann et al. (2024), which are larger ($96 \times 96 \times 64$) than the testing samples ($64 \times 64 \times 64$). Following their procedure, we apply random on-the-fly crops and rotations during training. We then further reduce the samples by keeping only the 8 fluid cell layers directly above the terrain, resulting in a final topography-conforming training geometry of $64 \times 64 \times 8$.

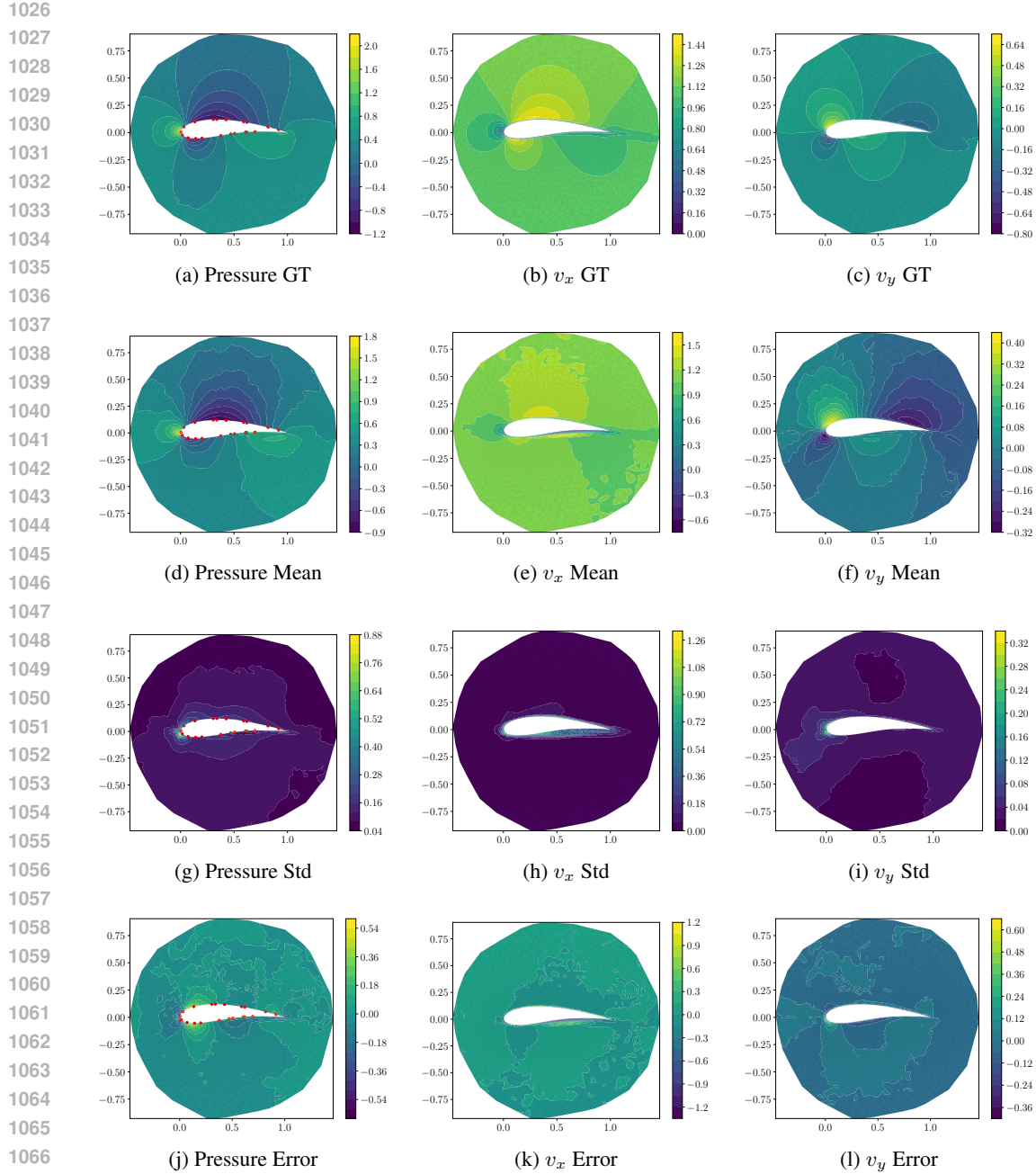


Figure 11: Comparison of ground truth (GT), inferred mean, error, and standard deviation for pressure (p), horizontal velocity (v_x), and vertical velocity (v_y). Columns group physical variables; rows show different prediction outputs.

Pred: At inference time, we decode 50k samples in batches of 40 samples, distributed over 4 GPUs, which takes around 480 seconds. We keep 100 samples as being drawn from the posterior.

B.6.2 ADDITIONAL RESULTS

In Figure 16 we show some examples of flows over different terrain geometries taken from the training set. In Figure 17 we show four random samples drawn from the generative prior model for a given terrain geometry, demonstrating the physical coherence and diversity of the prior. Due to the

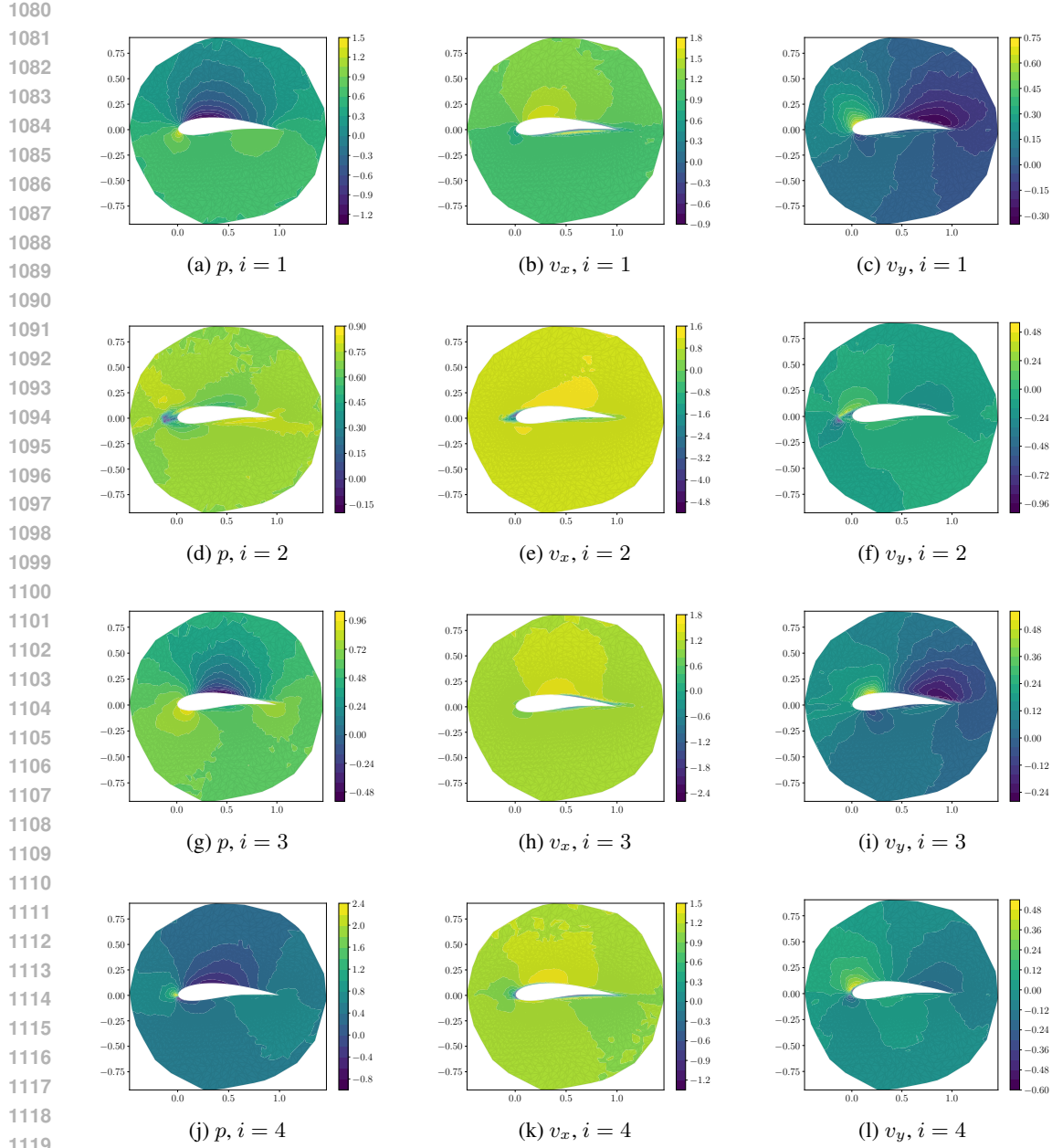


Figure 12: Airfoil field samples drawn from the geometry conditioned joint prior over pressure, v_x , and v_y generated as $\mathbf{u}_i \sim D_n^\psi q_{\mathbf{z}}$

nature of the training data (inflows from all directions are possible), the generated samples are more diverse in nature than the previous numerical setups.

C DISCUSSION ON VAEs

C.1 ALTERNATIVE VARIATIONAL FORMULATIONS

In this work we propose to: first train an autoencoder to learn an informative prior in the latent space, second to sample from the posterior given observational data. At first glance, an alternative approach would be to forgo this two step approach and attempt to directly learn a probabilistic

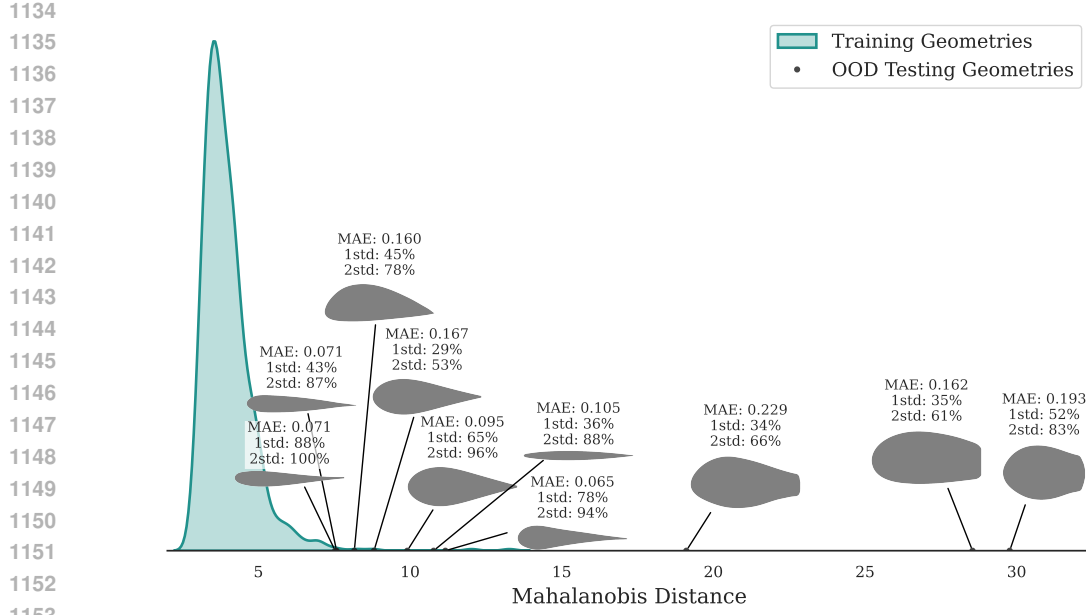


Figure 13: Out of distribution airfoil shapes and corresponding GABI inversion MAE and UQ for pressure, based on 20 observed airfoil nodes.

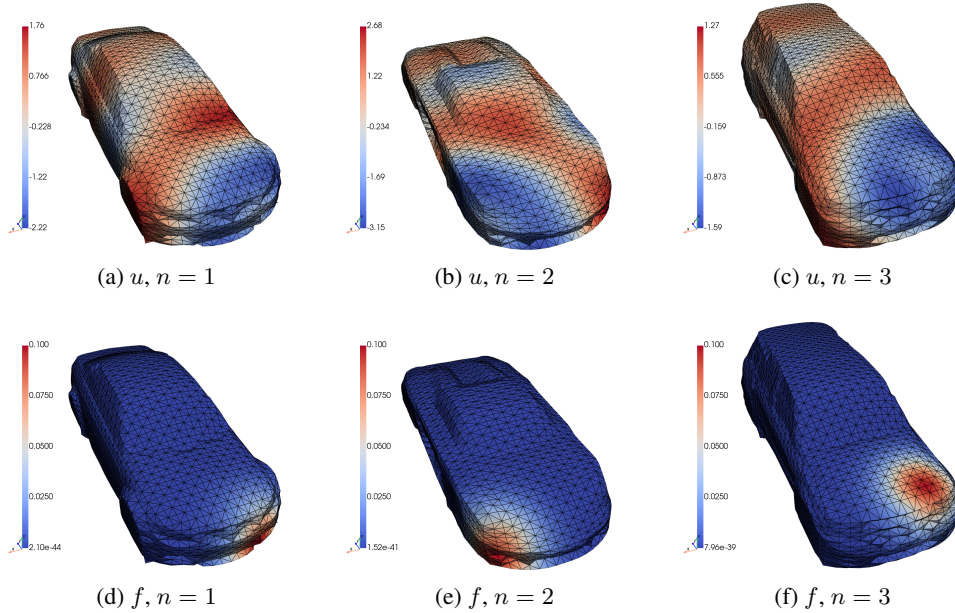


Figure 14: Three example meshes in dataset

geometry-conditional autoencoder in the form of a VAE

$$\theta^*, \psi^* = \arg \min_{\theta, \psi} \mathbb{E}_{\mathcal{D}_y} \text{KL} \left(q_{\mathbf{z}|\mathbf{y}_n}^{\theta} \| p_{\mathbf{z}|\mathbf{y}_n}^{\psi} \right), \quad (11)$$

$$\text{KL} \left(q_{\mathbf{z}|\mathbf{y}_n}^{\theta} \| p_{\mathbf{z}|\mathbf{y}_n}^{\psi} \right) = \log p_{\mathbf{y}_n}(\mathbf{y}_n) + \mathbb{E}_{q_{\mathbf{z}|\mathbf{y}_n}^{\theta}} [-\log p_{\mathbf{y}_n|\mathbf{z}}^{\psi}(\mathbf{y}_n)] + \text{KL} \left(q_{\mathbf{z}|\mathbf{y}_n}^{\theta} \| q_{\mathbf{z}} \right). \quad (12)$$

Upon close inspection of the loss for such a model, it is apparent that information from the full solution field \mathbf{u}_n is not incorporated in the learning, hence one cannot hope to learn the correct relationship between \mathbf{y}_n and \mathbf{u}_n .

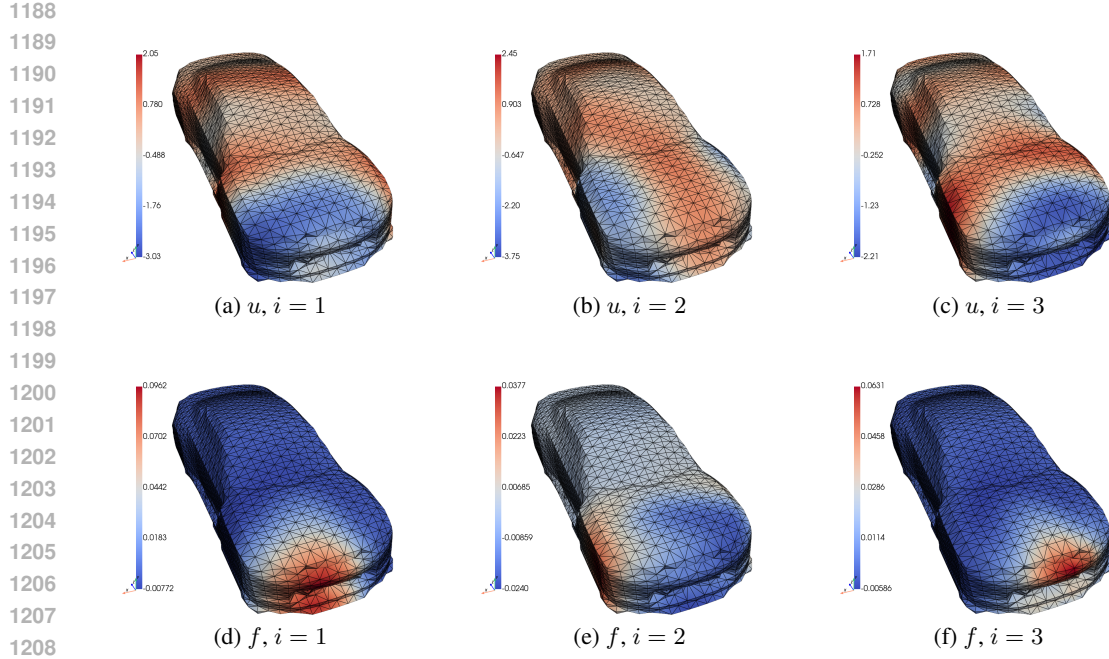


Figure 15: Given a geometry, we show 3 samples from the conditional prior generated as $\mathbf{u}_i \sim D_{n\#}^\psi q_{\mathbf{z}}$

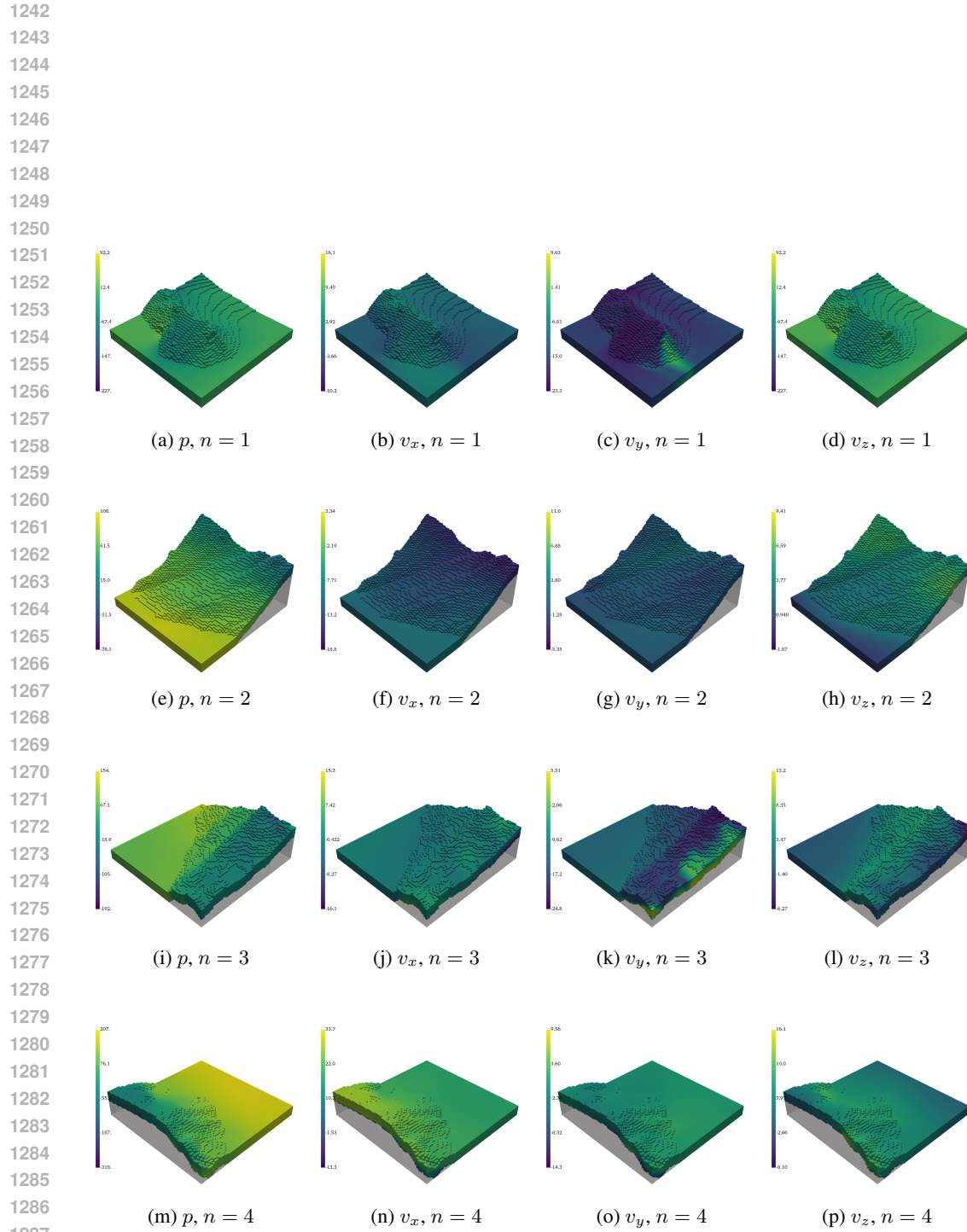
On could alternatively train a model of the form

$$\theta^*, \psi^* = \arg \min_{\theta, \psi} \mathbb{E}_{\mathcal{D}_y} \text{KL} \left(q_{\mathbf{u}_n | \mathbf{y}_n}^\theta \| p_{\mathbf{u}_n | \mathbf{y}_n}^\psi \right). \quad (13)$$

However, as \mathbf{u}_n are each associated with different geometries \mathcal{M}_n we cannot put a common prior distribution over these in a statistically interpretable manner. Furthermore, such a model would not learn the correct relationship between \mathbf{y}_n and \mathbf{u}_n as observational data is ingested in an unsupervised manner; no regression loss encourages \mathbf{y}_n to be close to \mathbf{u}_n in any way.

There exist other models such as UQ-VAEs (Goh et al., 2022) where the decoder is replaced by the solution operator for the assumed PDE responsible for generating the data. This of course requires us to know the governing of the problem, the boundary conditions etc – and has the same challenges and limitations as other physics-informed methodologies. Furthermore, this framework is not made to handle variable geometries.

C.2 VAEs INSTEAD OF REGULARIZED AUTOENCODERS

Figure 16: Four examples of flows (p, v_x, v_y, v_z) over complex terrain taken from the training set.

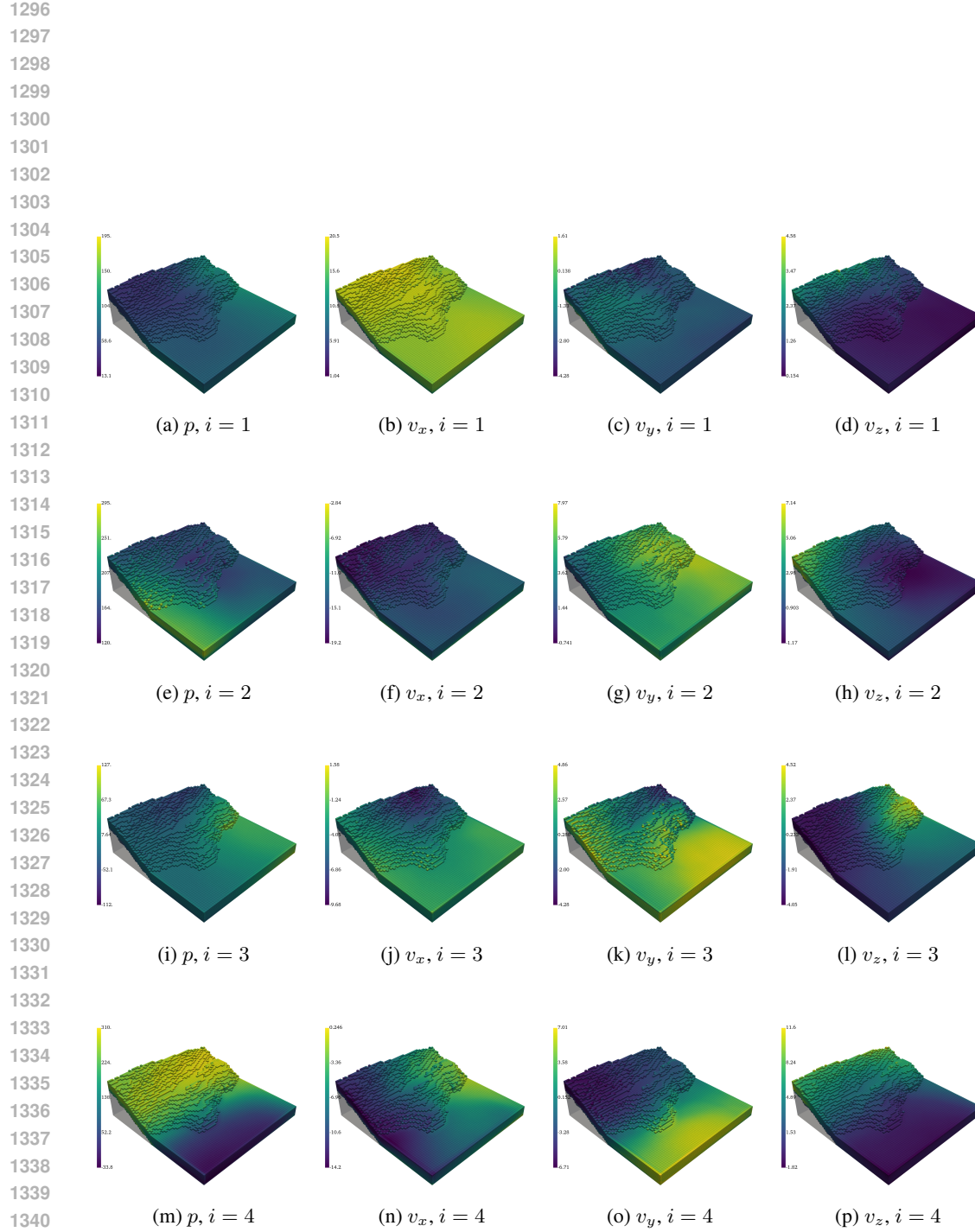


Figure 17: Flow field samples for a given test terrain drawn from the geometry conditioned joint prior over p, v_x, v_y , and v_z , generated as $\mathbf{u}_i \sim D_{n \#}^{\psi} q_{\mathbf{z}}$